Thermal annealing behavior of nano-size metal-oxide particles synthesized by ion implantation in Fe-Cr alloy

C. Zheng, A. Gentils, J. Ribis, V.A. Borodin, M. Descoins, D. Mangelinck, F. Dalle, B. Arnal, L. Delauche

Thermal annealing behavior of nano-size metal-oxide particles synthesized by ion implantation in Fe-Cr alloy

C. Zheng, A. Gentils, J. Ribis, V. A. Borodin, M. Descoins, D. Mangelinck, F. Dalle, B. Arnal, and L. Delauche

Citation: Journal of Applied Physics **121**, 174305 (2017); doi: 10.1063/1.4982756
View online: http://dx.doi.org/10.1063/1.4982756
View Table of Contents: http://aip.scitation.org/toc/jap/121/17
Published by the American Institute of Physics

Thermal annealing behavior of nano-size metal-oxide particles synthesized by ion implantation in Fe-Cr alloy

C. Zheng,[1,a)] A. Gentils,[1,b)] J. Ribis,[2] V. A. Borodin,[3,4] M. Descoins,[5] D. Mangelinck,[5] F. Dalle,[2] B. Arnal,[2] and L. Delauche[1]
[1]*CSNSM, Univ. Paris-Sud, CNRS/IN2P3, Université Paris-Saclay, Orsay, France*
[2]*DEN-Service de Recherches Métallurgiques Appliquées, CEA, Université Paris-Saclay, Gif sur Yvette, France*
[3]*NRC Kurchatov Institute, Kurchatov Sq., 1, 123182 Moscow, Russia*
[4]*NRNU MEPhI, Kashirskoe sh. 31, 115409 Moscow, Russia*
[5]*IM2NP, Univ d'Aix-Marseille, CNRS, Marseille, France*

(Received 16 February 2017; accepted 18 April 2017; published online 4 May 2017)

Oxide dispersion strengthened (ODS) steels are promising structural materials for the next generation nuclear reactors, as well as fusion facilities. The detailed understanding of the mechanisms involved in the precipitation of nano-oxides during ODS steel production would strongly contribute to the improvement of the mechanical properties and the optimization of manufacturing of ODS steels, with a potentially strong economic impact for their industrialization. A useful tool for the experimental study of nano-oxide precipitation is ion implantation, a technique that is widely used to synthesize precipitate nanostructures in well-controlled conditions. Earlier, we have demonstrated the feasibility of synthesizing aluminum-oxide particles in the high purity Fe-10Cr alloy by consecutive implantation with Al and O ions at room temperature. This paper describes the effects of high-temperature annealing after the ion implantation stage on the development of the aluminum based oxide nanoparticle system. Using transmission electron microscopy and atom probe tomography experiments, we demonstrate that post-implantation heat treatment induces the growth of the nano-sized oxides in the implanted region and nucleation of new oxide precipitates behind the implantation zone as a result of the diffusion driven broadening of implant profiles. A tentative scenario for the development of metal-oxide nano-particles at both ion implantation and heat treatment stages is suggested based on the experimental observations. *Published by AIP Publishing*. [http://dx.doi.org/10.1063/1.4982756]

I. INTRODUCTION

Oxide dispersion strengthened (ODS) steels, which are steels reinforced with dispersions of nanosize metal oxides, are promising structural materials for future nuclear and fusion reactors. The detailed understanding of the mechanisms involved in the precipitation of these nano-oxides would strongly contribute to the improvement of the mechanical properties and the optimization of manufacturing of ODS steels, with a potentially strong economic impact for their commercialization.

There is a growing body of evidence that the formation of metal-oxide particles (even of the most thermally stable oxides, such as Y_2O_3) during the standard ODS steel fabrication route involves the enrichment of the steel powder with alloying metal and oxygen at the powder milling stage, followed by co-precipitation of the dissolved metal and oxygen atoms during subsequent high-temperature/high-pressure powder sintering.[1] However, many details of precipitation kinetics remain unclear. Although some authors correlate the nucleation of oxide particles with their core/shell structure (e.g., Refs. 2 and 3), the others suggest particle nucleation to be initiated by substitutional oxygen atoms captured on vacancies.[4,5] There is a strong demand for experimental studies oriented on the elucidation of the mechanisms of oxide precipitation, in contrast to much more common works devoted to characterizations of ODS probes obtained with that or other technological approach.

With this in mind, we initiated recently a series of investigations devoted to the clarification of microstructural mechanisms of oxide particle nucleation and growth.[6,7] In order to have a clear picture of the precipitation kinetics, we deliberately eliminate many secondary factors that substantially complicate both experimental observations and their interpretation. First of all, instead of the standard techniques of ODS steel fabrication, we use a much more straightforward and well controlled approach of ion beam synthesis (IBS) that combines ion implantation at room temperature with a subsequent annealing at high enough temperatures to promote the precipitation of implanted species. The technique is widely used to synthesize precipitate nanostructures in well-controlled conditions, especially in microelectronics research and industry. As applied to metal-oxide particles in steels, the first attempt to create oxide particles by IBS seems to be the study by Sakuma *et al.*,[8] who have demonstrated the feasibility of creating yttrium-oxide nanoparticles by sequential implantation of yttrium and oxygen ions into unspecified ferritic alloys. Even though looking quite different from the conventional ODS steel fabrication techniques, ion implantation reproduces the relevant conditions, such as

[a)]Now at North Carolina State University, Raleigh, North Carolina 27695, USA. Electronic mail: czheng7@ ncsu.edu.
[b)]Author to whom correspondence should be addressed. Electronic mail: aurelie.gentils@csnsm.in2p3.fr. Tel.: +33 1 69 15 52 04.

the production of high vacancy concentrations. Second, even though yttrium and titanium are the metallic elements chosen nowadays to form metal-oxide particles, we prefer to deal with aluminum. In many aspects, Al_2O_3 precipitation is similar to that of yttrium oxide, but does not require so high temperatures to promote precipitation as Y_2O_3. Moreover, precipitation of aluminum oxides is of interest for a number of commercial ODS steels (e.g., MA956,[9] MA957,[10] and PM2000[11]) that contain Al as an important alloying element. Finally, we use for experiments a high-purity model Fe-Cr alloy, thus eliminating complicating effects from minor alloying elements (such as vanadium) that are contained in real steels and actively intervene in the initial stages of oxide precipitation.

Transmission electron microscopy (TEM) investigations revealed that the aluminum-based oxides appear in the Fe-10Cr matrix already upon ion implantation at room temperature.[6,7] This is quite uncommon for the ion beam synthesis approach, where high-temperature processing is typically applied after ion implantation to develop the nanoparticle ensemble. Among the other peculiar features were the metastable (cubic) crystal structure of precipitated particles and the clear orientational relation between crystal lattices of the particles and the host matrix. The detailed chemical analysis of particles indicated them to be a mixed (Al,Cr) oxide with a variable Al/Cr ratio, as revealed by the variations in the particle lattice parameters. The fact that the particles were able to precipitate at room temperature was rationalized in terms of radiation-accelerated mass transfer, which promoted the diffusion of the implanted Al and O ions.

Although Refs. 6 and 7 were focused on the investigation of the particle microstructure formed as a result of ion implantation, it was reasonable to expect that post-implantation annealing would promote the nucleation and growth of nano-precipitates. Moreover, it remained completely unclear, how annealing would influence the properties of nanoparticles, such as their crystal structure. This paper describes the results of our study on the development of aluminum-based oxide nanoparticle ensemble formed by ion implantation during subsequent annealing at 500 °C. We also report some earlier unpublished observations for as-implanted samples, the importance of which became clear for the proper treatment of the annealing results. Finally, we formulate a conceptual model of the oxide nucleation in IBS conditions that allows us to give a non-contradictory explanation of all our up-to-date experimental observations.

II. EXPERIMENTAL DETAILS

The as-received bulk material was a high-purity Fe-Cr alloy supplied by Ecole Nationale Supérieure des Mines, Saint-Etienne, France. Concentrations of major elements, according to the supplier's report, were 90.14 wt. % (89.46 at. %) for Fe and 9.86 wt. % (10.54 at. %) for Cr, respectively. Minor impurities, such as carbon, nitrogen, oxygen, and sulphur, were claimed to constitute less than 0.001 wt. %. Both Energy Dispersive X-ray spectroscopy (EDX) and Electron Energy Loss Spectrometry (EELS) were applied to verify chemical composition of the as-received material and confirm the high purity of this alloy.

The ion implantation procedure and measurement techniques were described in detail in Ref. 6 and are only briefly summarized here. Ion implantation was carried out at Centre de Sciences Nucléaires et de Sciences de la Matière (CSNSM/JANNuS-Orsay, France) with the Implanteur pour la Recherche en Métallurgie et en Astrophysique (IRMA) 190 kV ion implanter. Two-stage ion implantation was carried out, at room temperature, first with 70 keV Al^+ ions to the fluence of 2×10^{16} cm^{-2} and then with 37 keV O^+ ions to the fluence of 3×10^{16} cm^{-2}. The ion flux was 6.8×10^{12} cm^{-2} s^{-1} for both Al^+ and O^+ implantations. The ion energies were chosen using the SRIM software[12] so as to obtain ion distribution with a maximum implantation peak at 50 nm. The nominal (i.e., without the account of the diffusional broadening) peak concentrations, as estimated by SRIM, were 3.5 at. % for Al and 6.4 at. % for O atoms. The calculated damage production rates in the damage peak (at ~25 nm distance from the surface) are 1.027×10^{-2} and 5.35×10^{-3} dpa s^{-1} for Al^+ and O^+ ions, respectively, assuming the iron displacement threshold of 40 eV.[13] The specimen holder was inclined perpendicularly to the ion beam. In addition to the two-stage implantation experiment, a separate implantation with only Al^+ ion beam under the same conditions as in the two-beam experiment was undertaken in order to clarify whether the cluster formation starts already during the first implantation stage.

Transmission electron microscopes at CSNSM/JANNuS-Orsay and CEA-SRMA (Saclay) were used to perform the characterizations of nano-particles in both as-implanted and annealed specimens, using both conventional and analytical methods such as energy-filtered TEM (EFTEM) and high resolution TEM (HRTEM). The energy-filtered images were recorded using a binning of 2×2, thus resulting in 512×512 pixels. Elemental maps were acquired by using both three-window and jump-ratio methods, which are complementary to each other. For the three-window method, the parameters can be found in Ref. 6. For the jump-ratio method, the relevant iron peak in the low-loss region was 54 eV (Fe-$M_{2,3}$). Correspondingly, the window for the pre-edge acquisition started at 44 eV and the window for the post-edge acquisition started at 60 eV. For chromium, the relevant peak in the low-loss region is 42 eV (Cr-$M_{2,3}$), so the window for the pre-edge acquisition started at 32 eV and that for the post-edge acquisition—at 48 eV. For aluminum, which has the peak at 73 eV (Al-$L_{2,3}$), the window for the pre-edge acquisition started at 63 eV and that for the post-edge acquisition—at 78 eV. The used window widths were 8 eV for iron and chromium and 10 eV for aluminum.

The TEM thin foils were prepared by two methods: by a conventional mechanical and electrolytic polishing before ion implantation, as described in Ref. 6, and by the focused ion beam (FIB) using a standard cross-section preparation using an FEI Helios SEM/FIB dual beam microscope.[14] Both thin foil preparation methods produce similar results in terms of densities and sizes of nano-oxide particles.[14]

Thermal annealing was carried out inside the microscope at CSNSM using the *FEI* TEM heating specimen

holder. The annealing temperature was kept at 500 °C, and the total annealing time was 3 h, with TEM images taken in the middle of annealing at ~1 h after the annealing start. The initial heating ramp was at the rate of approximately 100 °C per minute. The vacuum condition inside the column of TEM was 1.2×10^{-5} Pa.

Atom Probe Tomography (APT) measurements were carried out using an atom probe (LEAP 3000^{TM} XHR, Imago Scientific Instruments) operated in the pulsed laser mode at IM2NP in Marseille, France. The tips were produced by an *in-situ* lift-out method using an FEI Helios 600 NanoLab 2–30 kV FIB. Prior to FIB tip preparation, a thin capping layer of sputter-coated nickel was deposited on the sample surface to prevent the tip damage by gallium ion beam. During the analysis, the specimen base temperature was maintained between 53 and 87 K in ultra-high vacuum conditions ($<1.7 \times 10^{-11}$ Torr). The laser energy varied from 0.5 to 1.2 nJ under a laser pulsing mode. Only runs exceeding 10^7 ions were considered in order to reduce the statistical error. The three-dimensional reconstruction of the sharp tip from APT data was done according to the methodology described in Refs. 15 and 16, using a commercial software (IVAS^{TM}) and an evaporation field close to the one of Fe (around 30 eV/nm). In order to characterize the nature (size, number density, distribution, and chemical compositions) of precipitates prior to and after thermal annealing, the cluster analysis technique suggested in Refs. 17 and 18 was applied with the parameter set $d_{\max} = 1.25$ nm, $N_{\min} = 30$, $L_{env} = 1.25$ nm, and $d_{erode} = 1$ nm (for the meaning of parameters, see the cited papers). Since the observed clusters are often of rather irregular form, the "size" of each individual cluster is determined in terms of the "effective" radius, R_G, defined in the IVAS software as

$$R_G = \sqrt{\frac{5}{3N}\sum_{n=1}^{N} |\boldsymbol{R}_n - \bar{\boldsymbol{R}}|^2},$$

where N is the number of atoms in the cluster, $\boldsymbol{R}_n$—the measured radius-vector of the n-th atom, and $\bar{\boldsymbol{R}}$—the average over all atom radius-vectors in the cluster (the cluster's center position). The cluster size determined in this way is known to be comparable with the size estimated by other analysis techniques such as the TEM characterization.[19] The mass spectra in the annealed APT sample were obtained directly during APT measurements, being extracted from the raw data by selecting the considered species.

III. RESULTS

As already said, the ion beam synthesis is typically done in two sequential stages, that is, room temperature ion implantation and subsequent high-temperature thermal annealing. In the current experiment, the oxide precipitation started already during the ion implantation stage. Because many results concerning the precipitate ensemble characterization after ion implantation (including cluster crystal structure, lattice alignment, and chemical composition) have already been published,[6,7] in Sec. III A, we restrict ourselves to the description of only new results that were obtained by more thorough inspection of as-implanted samples when the above-mentioned papers were already in press. The effects of annealing on the oxide particle system are described separately in Sec. III B.

A. The characterization of nano-particles in the as-implanted samples

1. Correlation of particle precipitation with the extended defects

The formation of (Al,Cr) oxide particles at the ion implantation stage cannot be explained without assuming relatively high room temperature mobility of Al and O atoms, well above the thermal one. Theoretical estimates indicated that the necessary rate of impurity transfer can be reasonably explained in terms of radiation-enhanced diffusion (RED),[6] but it were important to find also experimental indications of fast implant mass transfer. A definite indication for the efficient element transfer was the EFTEM observation of the radiation-induced segregation (RIS) on a grain-boundary in as-implanted specimens.[7] A more detailed study has confirmed the presence of RIS at different grain boundaries, as evidenced by EFTEM elemental maps in Fig. 1. The dark contrast on Fe-$L_{2,3}$ edge elemental maps, see Figs. 1(a) and 1(d), indicates local Fe deficiency at grain boundaries. Cr-$L_{2,3}$ edge and Al-K edge elemental maps (Figs. 1(b) and 1(c)) reveal the enrichment of Cr and Al at the same grain boundary. Oxygen and aluminum atoms are found to agglomerate at another grain boundary according to the O-K and Al-K elemental maps (Figs. 1(e) and 1(f)).

Having in mind the segregation of aluminum and oxygen atoms at extended defects, it is natural to expect the preferential nucleation of precipitates at sinks. Indeed, the precipitation of Al-rich clusters at grain boundaries was observed already after the Al implantation stage in the supplementary experiment without subsequent oxygen implantation; see Fig. 2. Unfortunately, due to relatively large grains in the implanted sample ($\geq 5\ \mu$m), we could not locate an appropriate grain boundary decorated with precipitates in the samples studied immediately after two-stage Al + O implantation, but there is little doubt that the Al-rich clusters at grain boundaries convert into oxide particles upon oxygen implantation.

Having in mind that RIS can occur at different kinds of sinks, conventional TEM observations were also applied to dislocation lines and loops, which were much easier to detect in as-implanted specimens after the two-beam implantation that grain boundaries. Fig. 3(a) shows a bright field (BF) TEM micrograph where large portions of dislocation lines are clearly visible. The corresponding dark field (DF) TEM micrograph (Fig. 3(c)), taken on the S1 diffraction spot circled in Fig. 3(b), shows exactly the same region of the as-implanted TEM thin foil as in Fig. 3(a). The precipitates, having the bright contrast, are clearly visible in Fig. 3(c) and in the zoom shown in Fig. 3(d). Their diameters vary from 3 to 15 nm, with the mean size of 5.5 nm. Remarkably, the precipitates are found to be located at the dislocation lines.

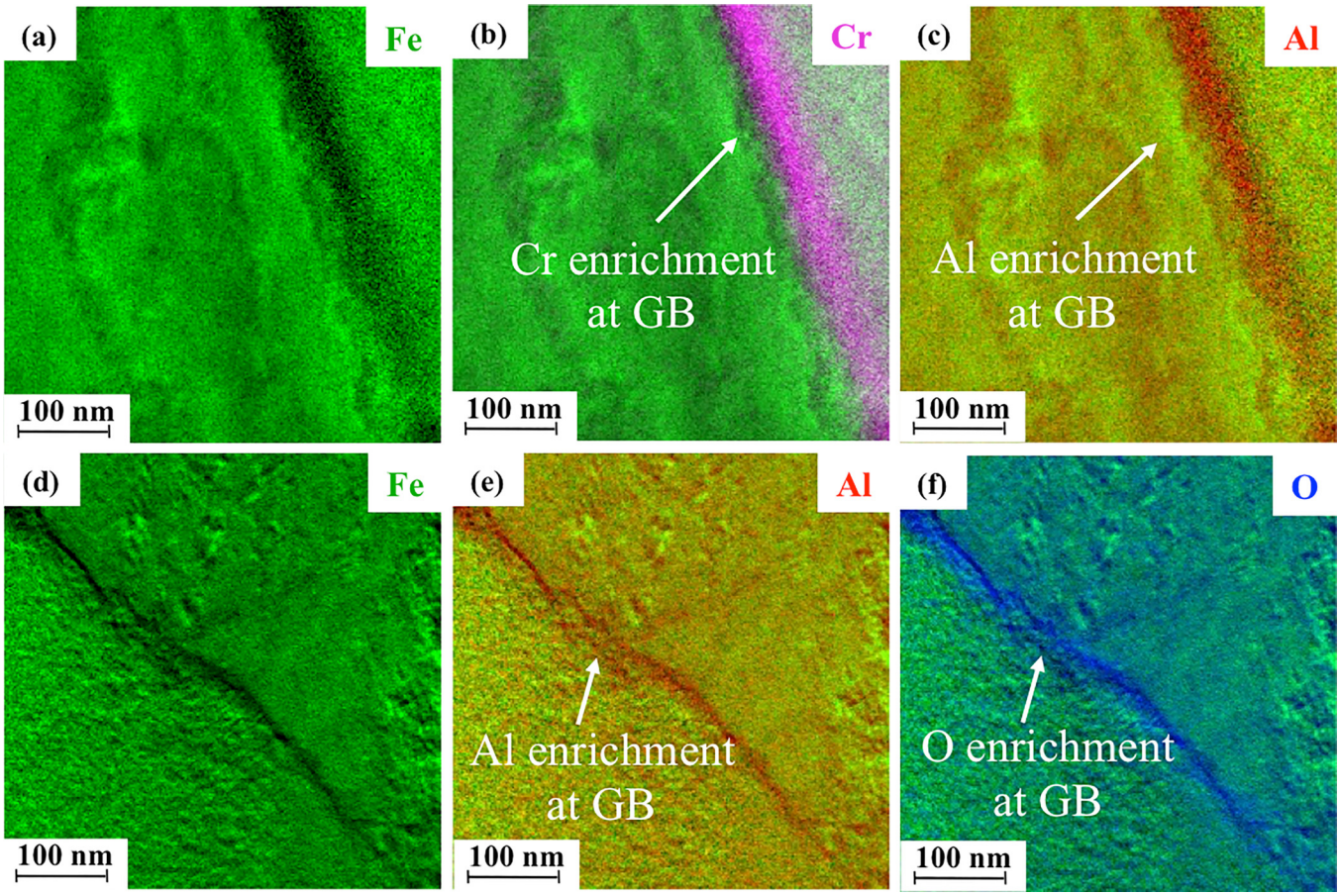

FIG. 1. EFTEM characterization at grain boundaries: (a)–(c) Fe, Cr, and Al three-window elemental maps acquired at one grain boundary, showing correlation between Fe depletion and Al-Cr enrichment. (d)–(f) Fe, Al, and O three-window elemental maps acquired at another grain boundary, showing correlation between Fe depletion and Al-O enrichment. The colors indicate the elements as marked in the legend.

In order to obtain better contrast for observing dislocation loops, the specimen was tilted to satisfy two-beam condition and studied by TEM, as shown in Fig. 4. The upper left panel shows a bright field TEM micrograph in which numerous dislocation loops can be noticed. The diffraction pattern in the inset confirms that the matrix is oriented along a ⟨111⟩ direction and the two-beam condition is fulfilled, enabling the white contrast of precipitates in the corresponding dark field TEM micrograph, shown in the lower left panel. Fig. 4 presents also enlarged bright- and dark-field images of four selected regions marked in the bright field TEM micrograph. The size of dislocation loops observed in these four regions is quite different, from 150 nm (regions 1, 2, and 3) down to 20 nm (region 4). The common feature is that precipitates decorate the dislocation loops. The precipitate sizes are typically very small (<5 nm) with only several slightly larger ones.

2. Chemical composition of nano-size oxide particles

a. EFTEM analysis. Precipitate chemical analysis has been performed using EFTEM imaging. The detailed EFTEM parameters used are described in Ref. 6. Before each EFTEM investigations, the foil thicknesses were calculated from EFTEM thickness maps by using the log-ratio method.[20] The inelastic mean free path of electrons was estimated from the equation derived by Malis.[21]

The typical outcome of EFTEM measurements performed in as-implanted thin foils is shown in Fig. 5. Fig. 5(a)

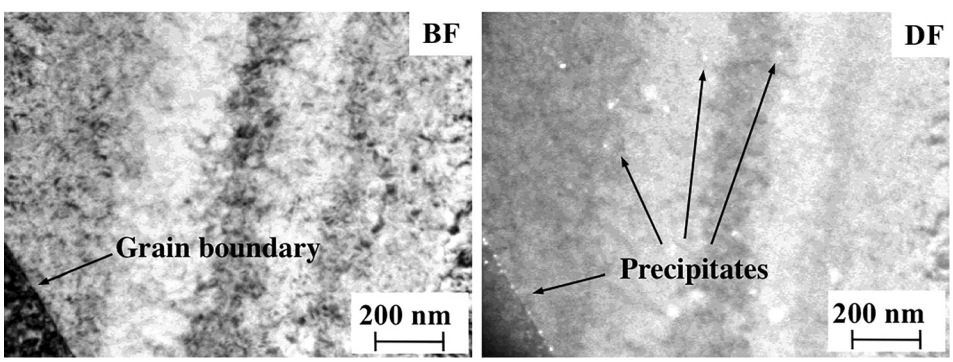

FIG. 2. The observation of precipitates at in the grain bulk and at grain boundary in the Al-only implanted sample. (a) Bright-field image. (b) Dark-field image. The arrows indicate the grain boundary and precipitates (shown as white dots in panel (b)), as explained in the legend.

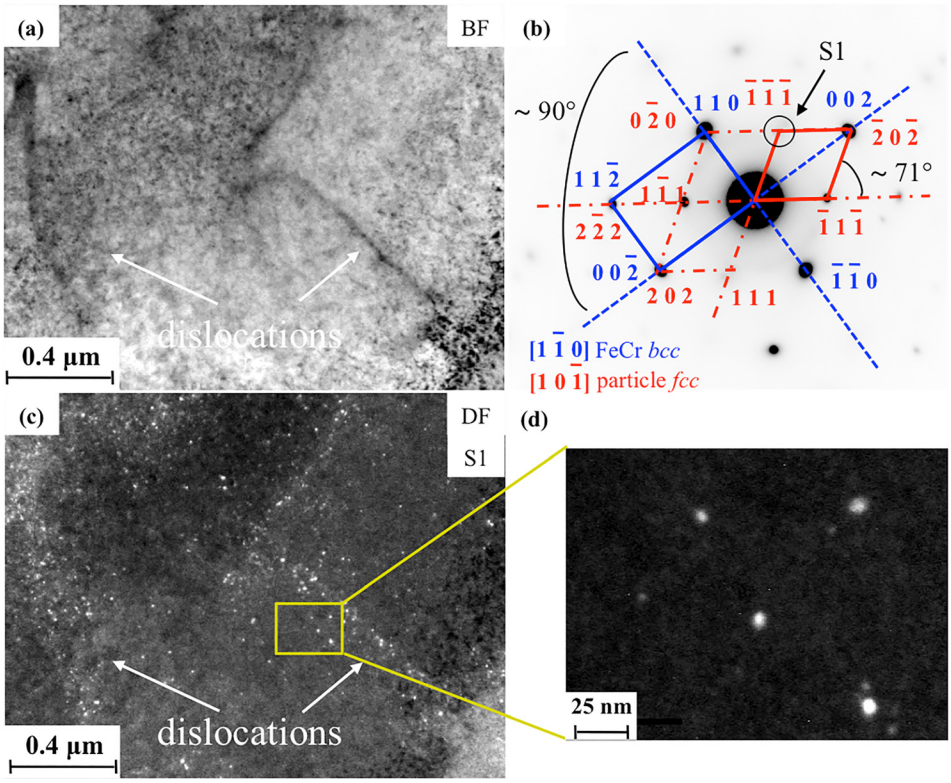

FIG. 3. TEM micrographs showing agglomeration of nano-particles on large portion of dislocation lines: (a) Bright field TEM micrograph in which some dislocation lines are clearly visible. (b) Electron diffraction pattern (negative level) for the region corresponding to (a). The particular zone axis orientation adopted for indexing the diffraction spots is specified in the legend. (c) Corresponding dark filed TEM micrograph obtained by taking the spot S1 in (b). (d) Detailed view of nano-particles.

is a bright field TEM image of a FIB lamina, which shows a typical spatial distribution of precipitates in the matrix. The dark contrasts are supposed to be precipitates and some of them are highlighted in panels (b)–(d) with white rectangles. The Fe-$M_{2,3}$ elemental map in Fig. 5(b) shows the local Fe depletion at the dark contrast areas in Fig. 5(a), whereas the enrichment in Al and Cr in the same areas is evidenced by bright areas in Figs. 5(c) and 5(d). An important conclusion from these observations is a substantially different role of Fe and Cr in the oxide precipitation. Chromium, in contrast to iron, is not evacuated from precipitate volume by accumulating Al and O atoms, remaining a constituent of the newly

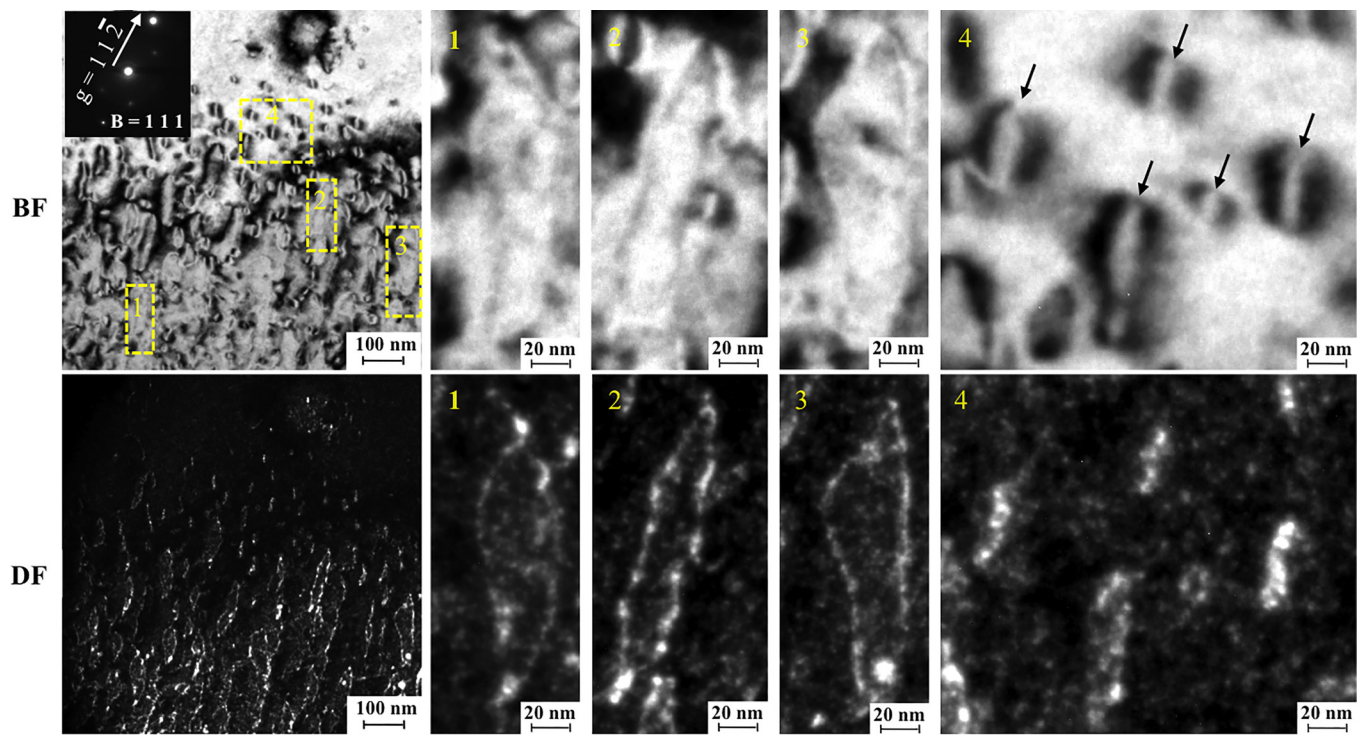

FIG. 4. TEM micrographs showing precipitation of nano-particles on dislocation loops. The upper row (from left to right): bright field TEM micrographs of the global view and zoom view of four different selected regions. The lower row: corresponding dark field TEM micrographs. The inserted diffraction pattern showing the specimen was tilted to satisfy two-beam condition ($s \approx 0$).

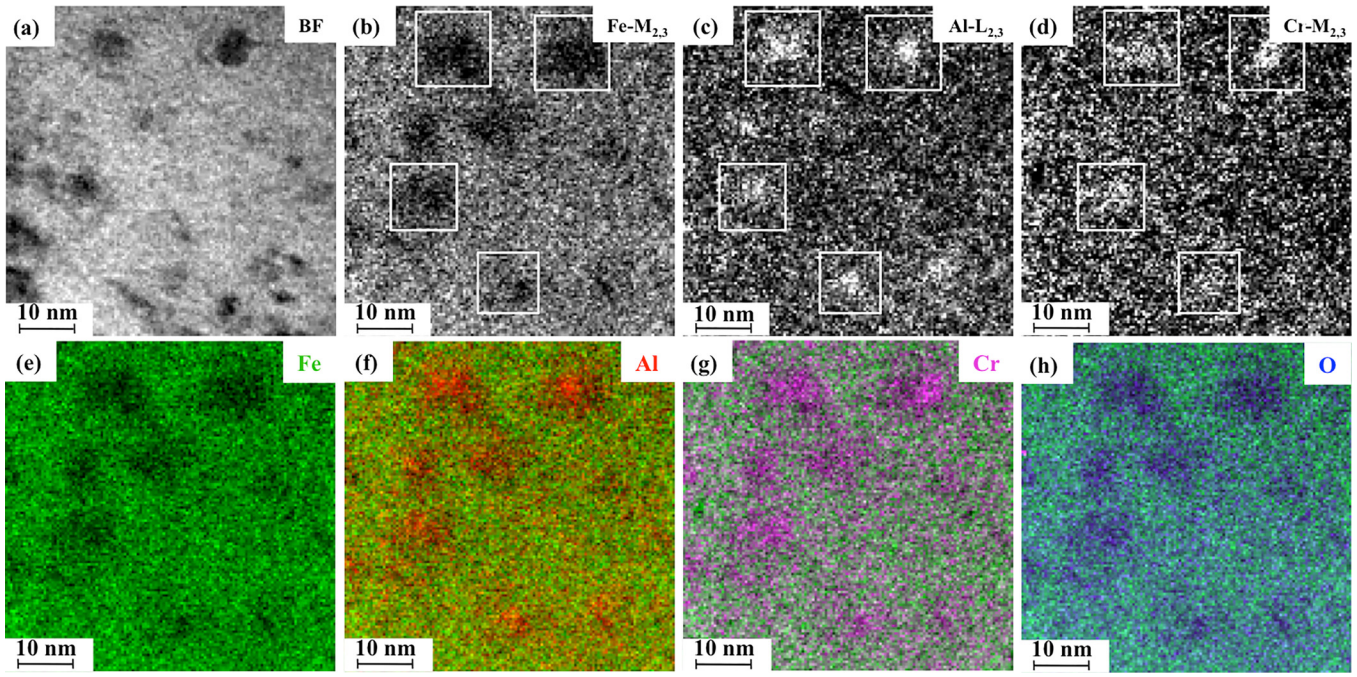

FIG. 5. EFTEM characterization of nano-particles: (a) bright field TEM image of the region of interest for the characterization. EFTEM jump ratio images acquired on Fe-$M_{2,3}$ (b), Al-$L_{2,3}$ (c), and Cr-$M_{2,3}$ (d) edges. The comparison among jump ratio images showing correlation between Fe depletion (e) and Al-Cr-O enrichment (f)–(h). The colors indicate the elements as marked in the legend.

formed precipitates. Moreover, the brighter contrast of Cr elemental map on the dark-contrast areas of Fe map indicates some chromium enrichment in precipitates as compared to the matrix (where its average content is ∼10 at. %), possibly as a result of local Cr transfer from the precipitate periphery. In order to better demonstrate the spatial relationships in the element distributions, Figs. 5(f)–5(h) present the "false color" Cr-$M_{2,3}$, Al-$L_{2,3}$, and O-K elemental maps superimposed over the Fe-$M_{2,3}$ map (Fig. 5(e), which is just a color version of Fig. 5(b)), as suggested in Ref. 22.

To be more quantitative, Fig. 6 shows the EFTEM scan of two nearby precipitates shown on a BF TEM image in panel (a). The intensity profiles reveal both Cr and Al enrichment in the particles. The O profile measurement (not shown) was less conclusive due to too high noise level induced, most probably by the oxidized sample surface. The sizes of precipitates measured from the intensity profiles are approximately 9 and 11 nm, respectively. It can be easily noticed that Cr and Al signal steps occur simultaneously, indicating the uniformity of Cr and Al distribution over the particles and the absence of the core-shell structure with Cr-rich outer shell, as is often reported for ODS particles. Another interesting feature is that the intensity step heights inside the precipitates for the Cr profile are essentially the same, whereas the Al signal intensity is clearly different. This provides an additional indication of the variability of Al/Cr ratio in precipitates.

Summing up, the EFTEM results justify our earlier suggestion[7] that the precipitates formed in as-implanted samples are (Al, Cr)-rich oxides with a variable Al/Cr ratio, rather than pure aluminum oxides, even if their chemical compositions are hard to determine quantitatively by EFTEM analyses.

b. APT measurements. More detailed conclusions concerning the relative contents of different precipitate constituents can be deduced from the reported below in-depth analysis of the APT measurements, already partly described in our earlier publication.[6] In brief, segregations of Al and O have been found in tips cut by the Focused Ion Beam (FIB) technique from relatively thick parts of an implanted TEM sample at the periphery of the beam spot. These segregations were too small (<2 nm in diameter) to be visible by TEM and were considered to correspond to the very early stages of oxide precipitation.

Elemental compositions were estimated for altogether 151 particles located at different depths in the range from 10 to 90 nm from the sample surface facing the beam. For all the studied clusters, the detected content of iron in the clusters was lower than the average iron content in the matrix at the same depth. On the other hand, the contents of Al and O in all the clusters are significantly higher than those in the matrix; see Fig. 7. The Cr content in precipitates fluctuates mostly within ±2 at. % around the average Cr value in the bulk, with ∼70% of the clusters having content of Cr higher than in the matrix.

The cluster enrichment in Al, Cr, and O, together with the depletion in Fe, is consistent with the results obtained in the as-implanted samples by EFTEM. In addition, the elemental composition of the clusters in the studied probe seems to be insensitive to the depth.

In spite of the evident cluster depletion in iron, the APT measurements indicate that iron remains the major constituent of the clusters identified in the as-implanted sample. However, the earlier studies[2,19] evidence that the level of iron in oxide particles, as measured by APT, can be strongly overestimated as a result of iron ion trajectory aberrations,

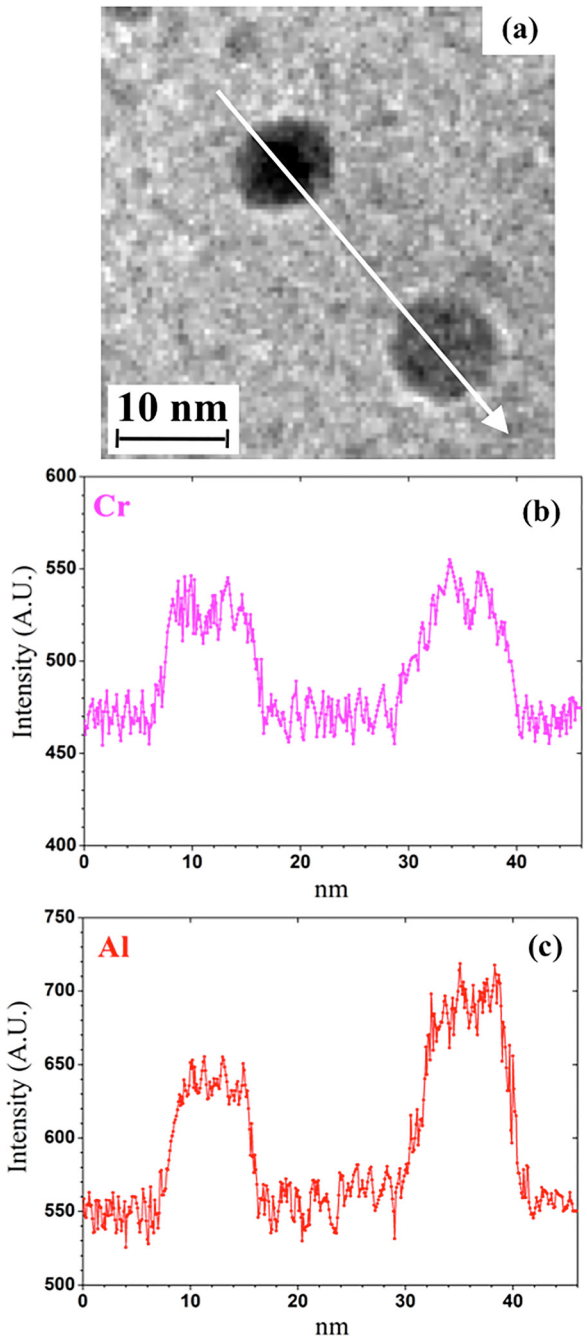

FIG. 6. (a) BF image of two precipitates in the as-implanted FIB lamina. (b), (c) Energy-filtered TEM scan through along the direction of the white arrow, showing the Cr and Al intensity profiles across the precipitates.

caused by the difference in the ionization field needed to evaporate the oxide particles and the surrounding matrix.[23] Indeed, distortions induced by trajectory aberrations were causing the reposition of matrix atoms up to several nanometers inwards of the particle/matrix interface even when particles were iron-free oxides.[19] In order to compensate for the aberration effects, the amount of Fe in clusters was forced to zero, whereas the relative content of other elements in the particles was corrected by calculating the likely proportion of these elements present together with iron in the matrix and removing this number from the raw cluster compositions, using the relation[2,19,24]

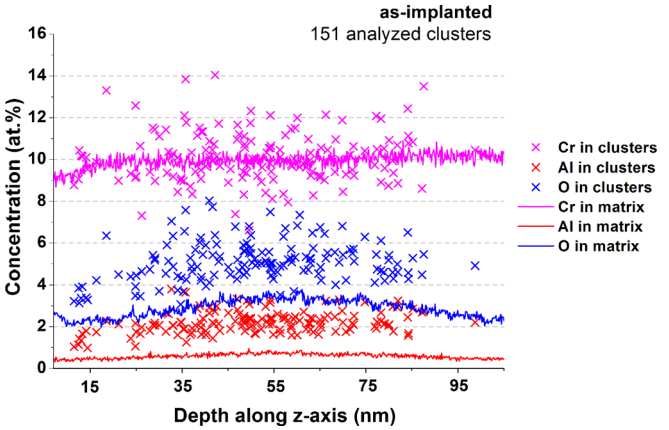

FIG. 7. The element contents in the matrix (oscillating solid lines) and in the analyzed clusters (crosses) as a function of the depth location of clusters. Colors for different elements are explained in the legend. The depth is measured from the interface between the sample and Ni capping layer used for the APT sample preparation by FIB.

$$c_i^c = c_i - (c_{\mathrm{Fe}}/C_{\mathrm{Fe}})C_i,$$

where c_i and c_{Fe} are the uncorrected contents of species i ($i =$ Al, Cr, O) and iron in the cluster, respectively, whereas C_i and C_{Fe} are the elemental contents in the matrix, respectively. The resulting values c_i^c are referred to below as matrix-corrected compositions.

The matrix-corrected compositions were estimated for all analyzed clusters, using the measured overall elemental content in the matrix, namely, 86.78 ± 0.03 at. % Fe, 10.06 ± 0.09 at. % Cr, 0.47 ± 0.09 at. % Al, and 2.69 ± 0.09 at. % O. The average values for the elemental content in clusters before and after the matrix-correction are listed in Table I.

In order to study the sensitivity of the Al/Cr ratio in clusters to the cluster size, the clusters in the as-implanted tip were sorted in the increase of their effective radius in the range from 1.6 to 4.4 nm with the bin width of 0.4 nm. The Al/Cr ratio in the as-implanted sample is weakly sensitive to cluster size both prior and after applying data correction, as shown in Figs. 8(a) and 8(b). However, the Al/Cr ratio has increased from 0.2 to 1.53 after the correction; see Table I. Even having in mind the very rough assumptions used in the correction procedure, it gives an indication that the ion trajectory aberrations in APT can strongly influence the estimation of the true contents of different metals in clusters. On the other hand, even though the ratio of oxygen to metal atoms in clusters has increased by the matrix correction from ~0.41 to ~0.83, the content of oxygen in small clusters detected by APT is well below the expected stoichiometry for an equilibrium $(Al,Cr)_2O_3$ compound.

3. Precipitate crystal structure

As already noticed earlier,[6,7] the crystallographic structure of the nano-oxide particles exhibits cubic symmetry, which does not correspond to the most stable (corundum) phase of either alumina, or (Al,Cr) oxide. This result has now been consistently reproduced using HRTEM on several tens of particles with sizes ranging from 3 to 15 nm. Three

TABLE I. The measured and matrix-corrected nanocluster compositions (at. %) in the investigated sub-volumes of the as-implanted and annealed specimens. The last two columns summarize the corresponding Al/Cr and O/(Al + Cr) ratios in the clusters.

	Fe	Cr	Al	O	Al/Cr	O/(Al + Cr)
As-implanted (Al + O) sample						
Uncorr.	82.64 ± 0.11	10.25 ± 0.24	2.10 ± 0.25	5.01 ± 0.25	0.21	0.41
Corr.	…	22.52 ± 0.35	34.5 ± 0.57	42.98 ± 0.59	1.53	0.83
After 3 h of annealing at 500 °C						
Uncorr.	80.15 ± 0.09	12.44 ± 0.19	3.98 ± 0.20	3.43 ± 0.20	0.32	0.21
Corr.	…	28.00 ± 0.30	41.06 ± 0.32	30.93 ± 0.31	1.47	0.45

typical examples of HRTEM images taken along [110], [001], and [111] axes are shown in Fig. 9. The lattice of the particles is interpreted as fcc (or based on the fcc pattern) with a lattice parameter varying in the range from 3.8 to 4.2 Å. Presumably, the variations in the lattice parameter reflect the different ratios of Al and Cr atoms on the metallic sublattice of oxide particles, being thus indicative of the variability of elemental content in precipitated particles.

The unusual lattice symmetry gives a hint that the precipitation of the aluminum and oxygen is strongly sensitive to the constraints imposed by the surrounding Fe-Cr alloy lattice. Additional evidence in favor of this conclusion is the visible correlation of the particle lattice orientation with the bulk lattice. An example of orientation relationship between the particle and the matrix can be inferred from Fig. 10(a), which shows the HRTEM image of a particle and the Fe-10Cr alloy matrix viewed along the same ⟨110⟩ direction, as identified from the Fast Fourier Transform (FFT) pattern in the upper right corner of Fig. 10(a). The distances and the orientation drawn in the lower right corner of Fig. 10(a) indicate that

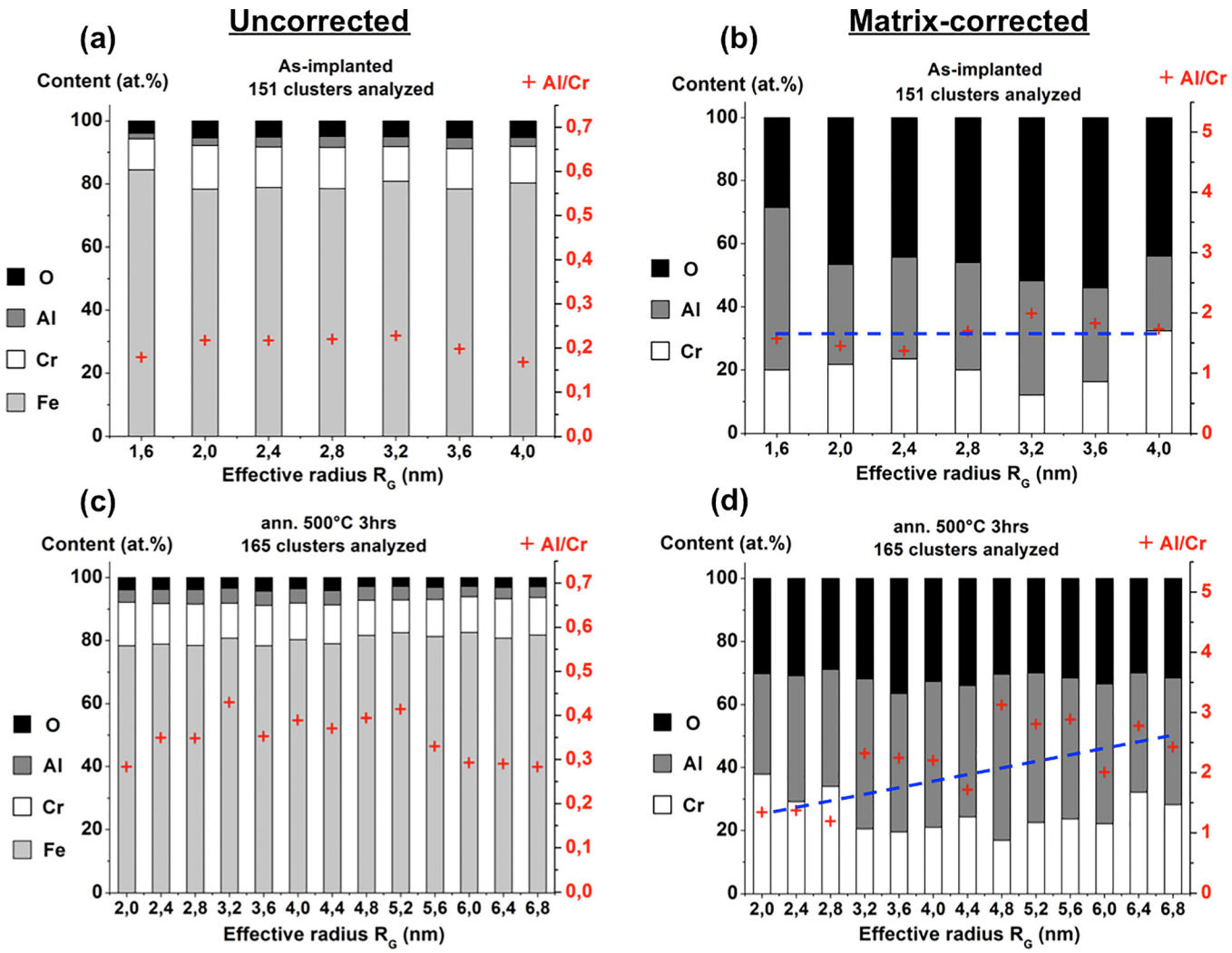

FIG. 8. The measured and matrix-corrected elemental contents in the clusters in (a), (b) the as-implanted APT tip and (c), (d) the annealed APT tip. Histograms are functions of the cluster effective radius. The columns in all panels correspond to the mesh of 0.4 nm, the gaps between columns are added to improve visibility. The average values of Al/Cr ratio in each size range are marked with red crosses. The blue dash lines are trend lines to guide the eye.

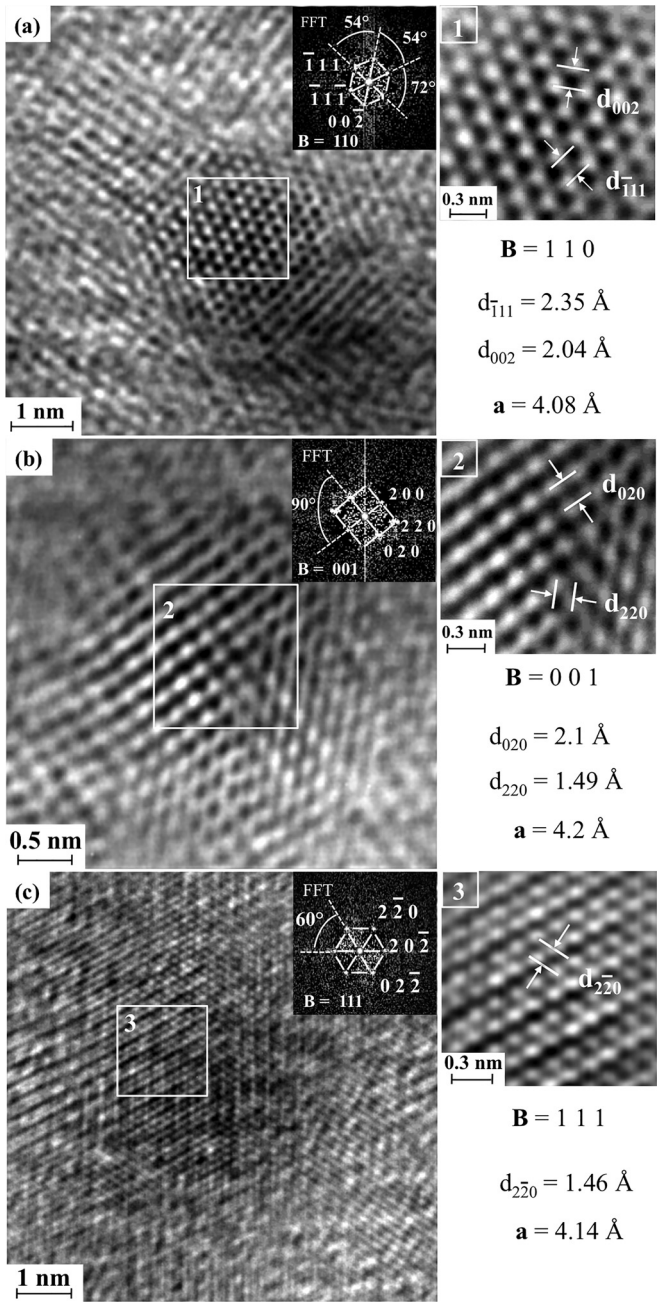

FIG. 9. Crystallographic structure of nano-particles: HRTEM images of three different nanoparticles along (a) [110], (b) [001], and (c) [111] axes. The corresponding fast Fourier transform (FFT) and magnified views of the nanoparticle HRTEM image are inserted in each case.

$[002]_{oxide}||[1\bar{1}0]_{Fe}$ and $[2\bar{2}0]_{oxide}||[00\bar{2}]_{Fe}$. Furthermore, the interplanar distances in the particle lattice are equal to those of the matrix in these directions. Both the particle and the matrix share zone axis ⟨110⟩ and appear to display a "cube on cube" orientation relationship, as schematically shown in Fig. 10(b). Note that such oxide lattice orientation with respect to the host lattice is very similar to that observed earlier for yttrium oxide particles in ODS steels.[25–27]

In order to get a better feeling concerning the possible crystal structure of the oxide particles, we have performed HRTEM simulations for some known cubic structures of aluminum and chromium oxide, trying to reproduce the HRTEM

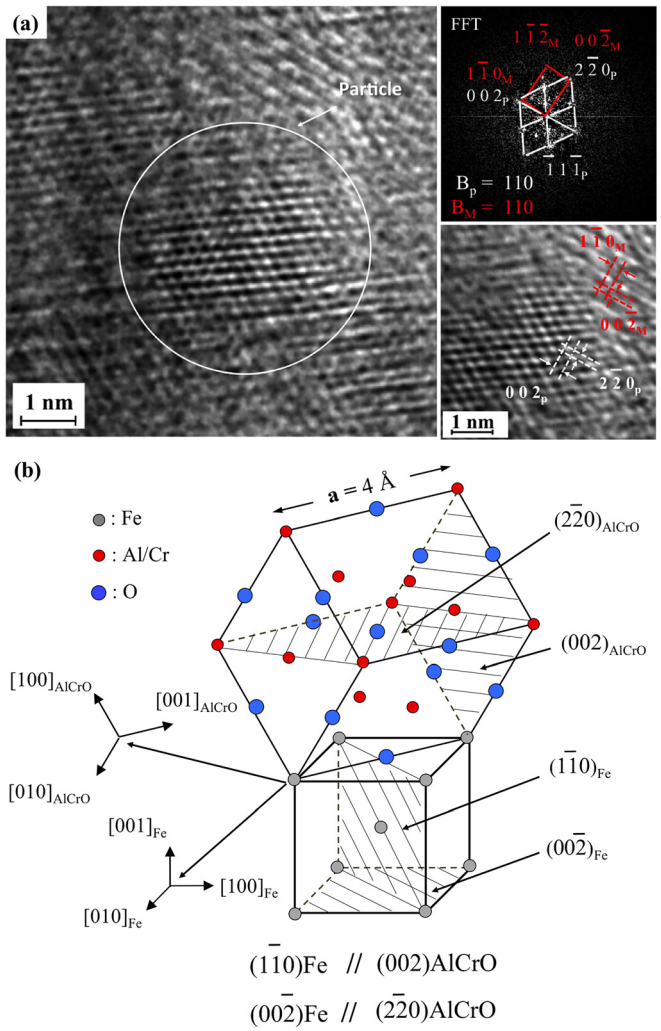

FIG. 10. Structure and coherency of nanoparticles: (a) HRTEM image of a nanoparticle along the [110] axis including a high-resolution detailed view of the interface and the corresponding fast Fourier transform (FFT). (b) Orientation relationships between matrix and nanoparticle.

patterns shown on the right-hand side panels of Figs. 9(a)–9(c) by adjusting TEM defocusing parameter within reasonable limits and considering the foil thicknesses below 20 nm. The simulations were done using the software package JEMS.[28] In particular, we tried spinel (which is commonly ascribed to cubic modifications of alumina[29]), perovskite, bixbyite, rocksalt, and a rocksalt-based structure suggested earlier for cubic Cr_2O_3.[30] The selection of defocus parameter, allowing the reproduction of experimental pattern for images along the ⟨100⟩ direction, was relatively simple for all considered structures. However, we were unable to reasonably reproduce the observed HRTEM pattern along the ⟨110⟩ direction for spinel, see Fig. 11(a), giving serious doubt that the particle crystal structure is that of spinel. Such conclusion is in agreement with the earlier experimental observations of cubic $(Cr,Al)_2O_3$,[31] where the spinel structure was definitely excluded. For the remaining studied structures, the ⟨110⟩ patterns are generally in agreement with that shown in Fig. 9(a), see Figs. 11(b)–11(e), though the fitting for perovskite is somewhat less perfect than for other structures. The first-principles calculations[32] demonstrate that the perovskite

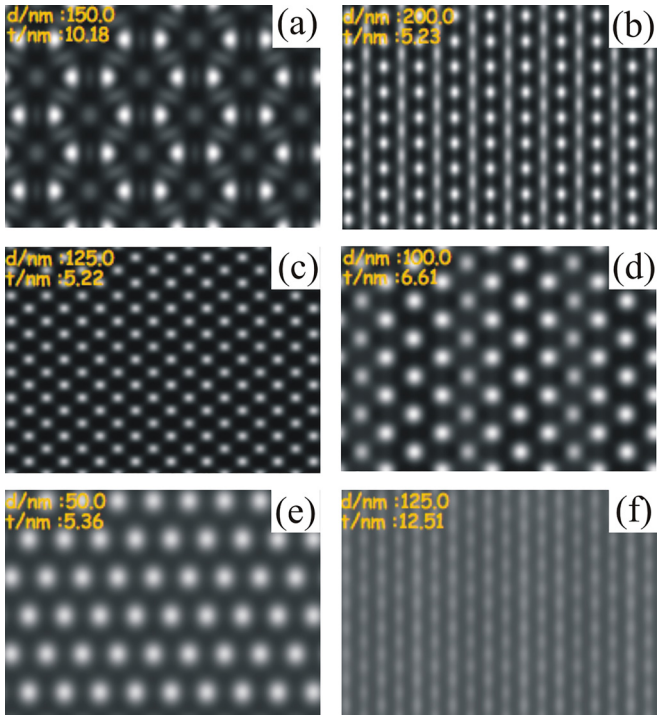

FIG. 11. Simulated HRTEM images along the ⟨110⟩ direction for different crystal structures: (a) spinel; (b) perovskite; (c) rocksalt; (d) bixbyite; (e), (f) rocksalt-based cubic structure suggested for cubic Cr_2O_3 in Ref. 30. The latter structure has one special ⟨110⟩ orientation with an HRTEM image looking as shown in panel (d).

structure for cubic (Al,Cr) oxide is not very energy profitable, at least as compared to the tentative rocksalt-based structure from Ref. 30, though this is not a sufficient ground to exclude it completely. The other three structures reproduce ⟨110⟩ images well. The only problem one meets with the rocksalt-based structure from Ref. 30 is its remarkable anisotropy in terms of metal atom positioning in the unit cell. As a result, one of six possible ⟨110⟩ directions (the one along the ordered rows of vacancies in the metal sublattice) gives the HRTEM pattern very different from the experimental one; see Fig. 11(f). Although such an anisotropy can be reasonable in a planar structure grown one-dimensionally, as was the case in the cited paper, it is hard to imagine how it arises in nanoclusters grown essentially three-dimensionally. Finally, although all the studied structures correctly predict the hexagonal spot pattern in the ⟨111⟩ direction HRTEM image, none of them could reproduce the periodic intensity variation of bright spot rows seen in the right panel of Fig. 9(c). Hence, it cannot be excluded that the crystal structure of the oxide particles is different from any of the structures considered in this work. Summing up, Fig. 11 demonstrates that the most obvious guesses for the crystal structure of precipitates do not give satisfactory agreement with the observations and more studies are needed to unequivocally identify it.

There may be different reasons for the crystal structure of observed particles to differ from the common cubic sesquioxide structures. First of all, there is no *a priori* guarantee that a perfect 2:3 ratio between metal and oxygen atoms is maintained in clusters, when they are only several nanometer large. Indeed, if the reasoning in Sec. III A 2 b is close to reality, the oxygen content in the nuclei of oxide precipitates would be typically at the level of 40–50 at. %. Having also in mind that the particles are quite rich in chromium, it is plausible that the small particle structure would be similar to that of CrO, which is known to be rocksalt.[33] And even for the stoichiometric $(Al_{1-x}Cr_x)_2O_3$ structures, several studies in the recent years reported the observation of cubic (Al, Cr) oxides with a rocksalt-based crystal structure[31,34–36] and studied their stability and properties theoretically.[32,37] Remarkably, a cubic phase $(Al_{1-x}Cr_x)_2O_3$ grew during the thin film epitaxial deposition at moderate temperatures (<600 °C) on cubic lattice substrates. In other words, the constraints imposed on the growing film from the substrate stabilize cubic structure, even though the latter is predicted to be less energetically favorable than the hexagonal corundum phase.[37] A similar situation takes place in our experiments, where the growth of precipitates is strongly constrained by the surrounding Fe-Cr alloy matrix. The lattice parameter of the cubic oxide phase observed in the above-mentioned experimental studies was slightly above 4 Å, also quite similar to our observations.

B. The evolution of the nano-particle ensemble under thermal annealing at 500 °C

The thermal annealing of implanted Fe-10Cr alloy samples at 500 °C in vacuum visibly modified the oxide particle nanostructure. An example TEM micrograph of the sample after 1 h annealing is shown in Fig. 12. A clear trend for oxide particle alignment in the grain bulk is visible, in agreement with the observed preferential precipitation at dislocations in as-implanted samples. One can also notice multiple precipitates at the grain boundary, though these are not much different in size from those in the bulk.

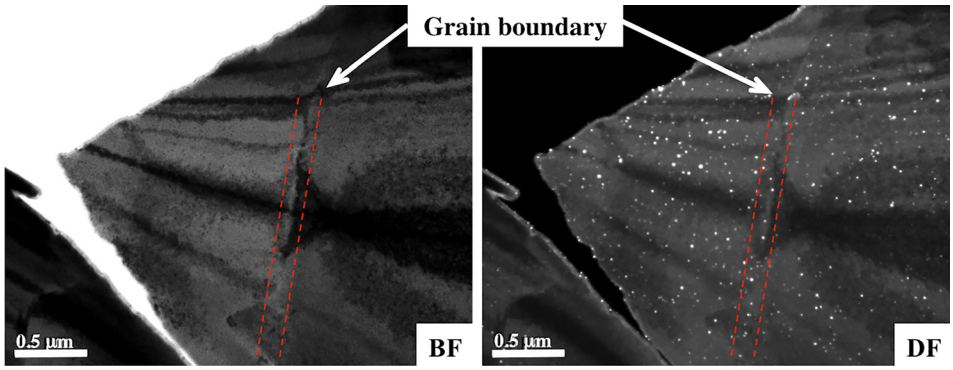

FIG. 12. (a) Bright field and (b) dark-field TEM micrographs of the sample implanted by Al and O ions at RT and subsequently annealed for 1 h at 500 °C. Precipitates are visible as white dots in panel (b). One can notice multiple precipitates at the grain boundary (marked by bracketing two red lines).

1. Diffusion acceleration of implanted atoms at 500 °C

An immediate consequence of the temperature increase should be the acceleration of diffusion of both aluminum and oxygen, leading to a broadening of the implanted ion depth profiles. Such broadening was indeed detected in the APT tip prepared from the annealed sample. Fig. 13(a) shows an example of the reconstructed elemental distribution for CrO fragments that are indicative of all internal oxides containing Cr, whereas Fig. 13(b) presents the measured depth-dependent concentration profiles for Al and O after the three hours annealing. As can be noticed in both panels, the outer sample surface was strongly oxidized during the annealing, with the large oxide clusters lying immediately under the oxidized surface, which were identified by diffraction measurements as the iron-chromium oxide.

For the purpose of comparison, the "as-implanted" profiles of Al and O calculated using the SRIM code are superimposed over Fig. 11(b). The superposition should be considered, however, with certain care. First of all, the depth coordinate reconstruction from APT results is sensitive to the measurement parameters. We believe that due to the use of classical parameters and the iron evaporation field, the reconstruction error is not large, but there are no exact criteria to verify the accuracy of the obtained depth scale. Second, due to the surface oxidation, the volume expansion takes place, which can be characterized by the so-called Pilling–Bedworth ratio (i.e., the ratio of the volume of the elementary cell of a metal oxide to the volume of the elementary cell of the corresponding metal).[38] Assuming the oxide layer to be magnetite (cubic spinel with unit cell $Fe_{48}O_{64}$ and lattice parameter 11.87 Å), it is easy to estimate the Pilling-Bedworth ratio to be close to 3. In other words, the original sample surface (prior to oxidation) was located at the depth of ~2/3 of the visible oxide thickness. So, with the observed oxide thickness of 20–25 nm, the SRIM profiles in Fig. 13(b) are shifted by ~15 nm from the interface "capping layer–oxide" deeper into the sample in order to compensate for the oxidation-induced volume expansion.

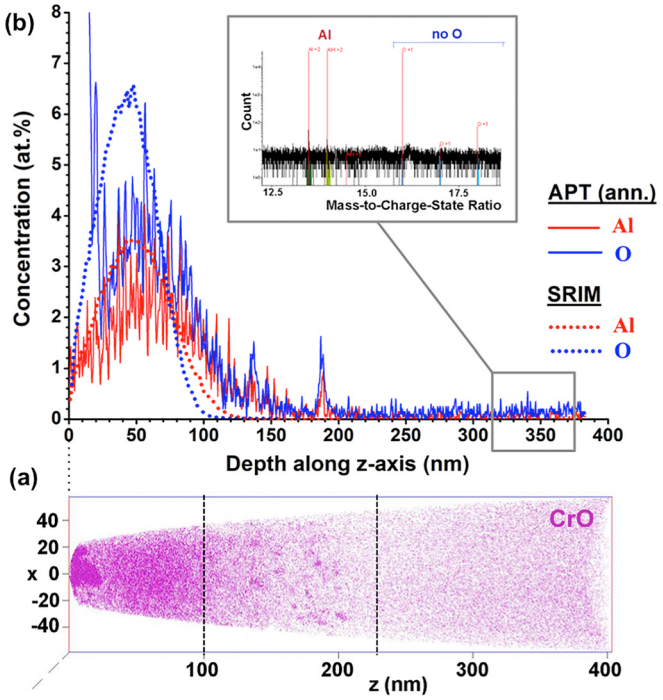

FIG. 13. (a) The reconstructed distribution of CrO fragments from APT analyzed tip cut from the annealed sample. Dash lines limit the zone used for cluster analysis. (b) The depth dependencies of 1-D concentration profiles for Al (red lines) and O (blue lines) obtained by the APT analysis in the annealed tip (solid lines) and from the SRIM simulation (dash lines). The inset shows the mass spectra measured in the range of 300 to 400 nm, demonstrating the presence of the Al peak and the absence of O at depths well behind the annealed profile.

With these considerations in mind, we can say that the depths of profile maxima for Al and O remain in place after the annealing. But the profile peak heights decrease after the annealing and the long profile tails extending till the end of the tip appear. The visible broadening of the implant profiles indicates that after the implantation stage, a large share of implanted aluminum and oxygen atoms remain dissolved in the matrix rather than consumed in precipitates formed at the ion implantation stage. These dissolved atoms are free to promote the growth of the existing particles and the nucleation of new oxide clusters at the annealing stage. An interesting feature observed in Fig. 13(b) is the correlated pick on both aluminum and oxygen profiles at 190 nm, which is clearly above the background (several similar, though less pronounced correlated peaks can also be seen at depths between 130 and 190 nm). The correlated peaks are most probably caused by small (Al,O)-rich clusters intercepted by the thin (10 nm in diameter) cylindrical region used to extract the element concentration profiles from APT data.

The observed broadening of aluminum and oxygen concentration profiles can be used to roughly estimate the "apparent" mobility of aluminum and oxygen atoms at the annealing stage. For this purpose, the concentrations profiles, $C(z)$, were approximated by Gaussian functions of the form

$$C(z) = C_p \exp(-(z - R_p)^2/4\sigma^2),$$

where z is the depth coordinate, R_p is the profile peak location, σ is the variance, and C_p are the value of implant concentration in the peak. For the concentration profiles after annealing, only the profile parts lying to the right of the profile maxima in Fig. 13 were used for fitting because they are not influenced by outer surface effects, in particular, thermal oxidation. Knowing the variation of the variance parameter as a function of time, t, one can determine the diffusion coefficient, D, from the known relation

$$\sigma^2(\mathrm{t}) = \sigma_0^2 + 4Dt,$$

where σ_0 is the variance at time $t = 0$. In our case σ_0 is assumed to be that for depth distribution predicted by SRIM.

The estimated variances for concentration profiles shown in Fig. 13 are $\sigma_0 = 20.15$ nm and $\sigma(3\mathrm{h}) = 29$ nm for aluminum and $\sigma_0 = 15.4$ nm and $\sigma(3\mathrm{h}) = 33$ nm for oxygen. This gives for the "apparent" diffusion coefficients

$$D_{\mathrm{Al}} = 3.8 \times 10^{-16}\mathrm{cm}^2/\mathrm{s} \quad \text{and} \quad D_{\mathrm{O}} = 6.3 \times 10^{-16}\mathrm{cm}^2/\mathrm{s}.$$

It should be kept in mind, however, that the implant profile broadening is affected by the aluminum and oxygen capture

at extended defects and by the oxide particle nucleation. So, it is instructive to compare the estimated "apparent" diffusion coefficients with those expected for aluminum and oxygen from the known literature data. The diffusion coefficients are commonly described in terms of Arrhenius relation

$$D = D_0 \exp(-E_m/kT),$$

where D_0 is a numerical prefactor, E_m is the migration barrier, k is the Boltzmann constant, and T is the absolute temperature. Table II below summarizes available information on the Al and O diffusion in iron and the measured or extrapolated values of their diffusion coefficients at 500 °C.

The migration barriers for Al atoms, where reported, are close to the self-diffusion energy barrier in iron. This is usual for substitutional impurities whose thermal diffusion is mediated by vacancies. Assuming that the presence of ~10 wt. % Cr only weakly affects the mobility of thermal vacancies, we expect that the aluminum diffusion coefficient in our case is close to that in pure iron. As can be seen, the literature data for the most cases predict the Al diffusion coefficient at 500 °C to be of the order of 10^{-16} cm^2/s, very similar to the value deduced from the Al profile broadening during the annealing.

On the other hand, two studies predict the Al diffusivity to be either much faster,[43] or much slower[41] than the value deduced in our experiment. Remarkably, both papers used an approach very similar to that of our study, that is ion implantation followed by annealing at high temperatures. Although the much lower value is definitely inconsistent with our observations, the accelerated Al diffusion in Ref. 43 was directly measured rather than extrapolated from higher temperatures and is most probably not an artifact. In fact, some indications of the fast diffusion of Al can also be observed in our case, because low, but reliably identifiable concentration of Al was found far behind the thermally broadened Gaussian profile in the annealed samples by APT measurements; see Fig. 13(b). Our earlier observations of the suppression of metal-oxide cluster precipitation in thicker parts of TEM samples can also be reasonably explained by the radiation-accelerated diffusion of Al already at the first stage of implantation (for a detailed discussion, see Ref. 6).

For O diffusion, several data sets are collected in Table II. In spite of different assumed oxygen mobility modes (as an interstitial or in an oxygen-vacancy complex) and quite different estimated diffusion coefficients at 500 °C, the predicted oxygen mobility is orders of magnitude larger than that estimated from the O profile broadening in the annealed sample. Moreover, in contrast to Al, no oxygen or O-related molecular ions are found on the mass-spectra measured by APT at depths well behind the annealed profile (see insert in Fig. 13(b)). Hence, it looks like the oxygen profile broadening at the annealing stage is limited not by the oxygen diffusion, but by some other processes at the nanolevel. Taking into account very similar depth dependences of oxygen and aluminum in Fig. 13, it may be tentatively suggested that the oxygen propagation into the sample is controlled rather by the oxygen trapping on the aluminum-vacancy and/or chromium-vacancy complexes that might further develop into oxide nanoclusters.

2. Precipitate size variation during thermal annealing

The thermal annealing leads to the visible ripening of oxide precipitates formed at the ion-implantation stage, as can be noticed in Fig. 14. The histograms presented in Figs. 14(e) and 14(f) highlight the precipitate size distribution changes after 1 and 3 h of annealing at 500 °C, respectively, as compared to the particle size distribution in the as-implanted sample. Although the average precipitate diameter, $\langle d \rangle$, in the as-implanted sample was measured to be ~4.3 nm, the 1 h annealing causes the increase of the average diameter to ~6.5 nm; after 3 h the average size further increases to ~7.7 nm, indicating the slowing down of particle growth with the annealing time. Assuming the power law kinetics for the precipitate size as a function of time t, $\langle d \rangle \propto t^n$, this would roughly correspond to $n \sim 0.4$. The growth of the average particle size is accompanied with the broadening of the size distribution as the annealing time increases.

In contrast to the precipitate size, the number density of precipitates in the areas where precipitates were observed in the as-implanted samples changes little during the annealing. Using the measured surface number density of precipitates and assuming the TEM sample thickness of 100 nm, the

TABLE II. The diffusion parameters (prefactor D_0 and migration energy E_m) for aluminum and oxygen, as well as the measured or extrapolated values for the diffusion coefficients at 500 °C.

D_0 (cm^2/s)	E_m (eV)	Temperature range (°C)	Evaluation technique	D (500 °C) (cm^2/s)	References
Aluminum					
		800–1050	In-diffusion from liquid Al	1.3×10^{-16}	39
50–100	2.67	800–1100	Al vapor in-diffusion	3.6×10^{-16}	40
1.6	3.17	775–900	40 keV Al ion implantation + annealing	3×10^{-21}	41
		300–500	25 keV Al ion implantation + annealing	2.5×10^{-14}	43
5.5	2.55			1.2×10^{-16}	42
Oxygen					
0.4	1.73	700–850	Internal oxidation	6.2×10^{-7}	44
2×10^{-3}	0.95	750–850	Internal oxidation	2.5×10^{-14}	45
1[a]	1.55	Below Curie temperature (770 °C)	First-principles calculations	7.5×10^{-11}	4

[a]An arbitrary value used to make the estimate in the fifth column

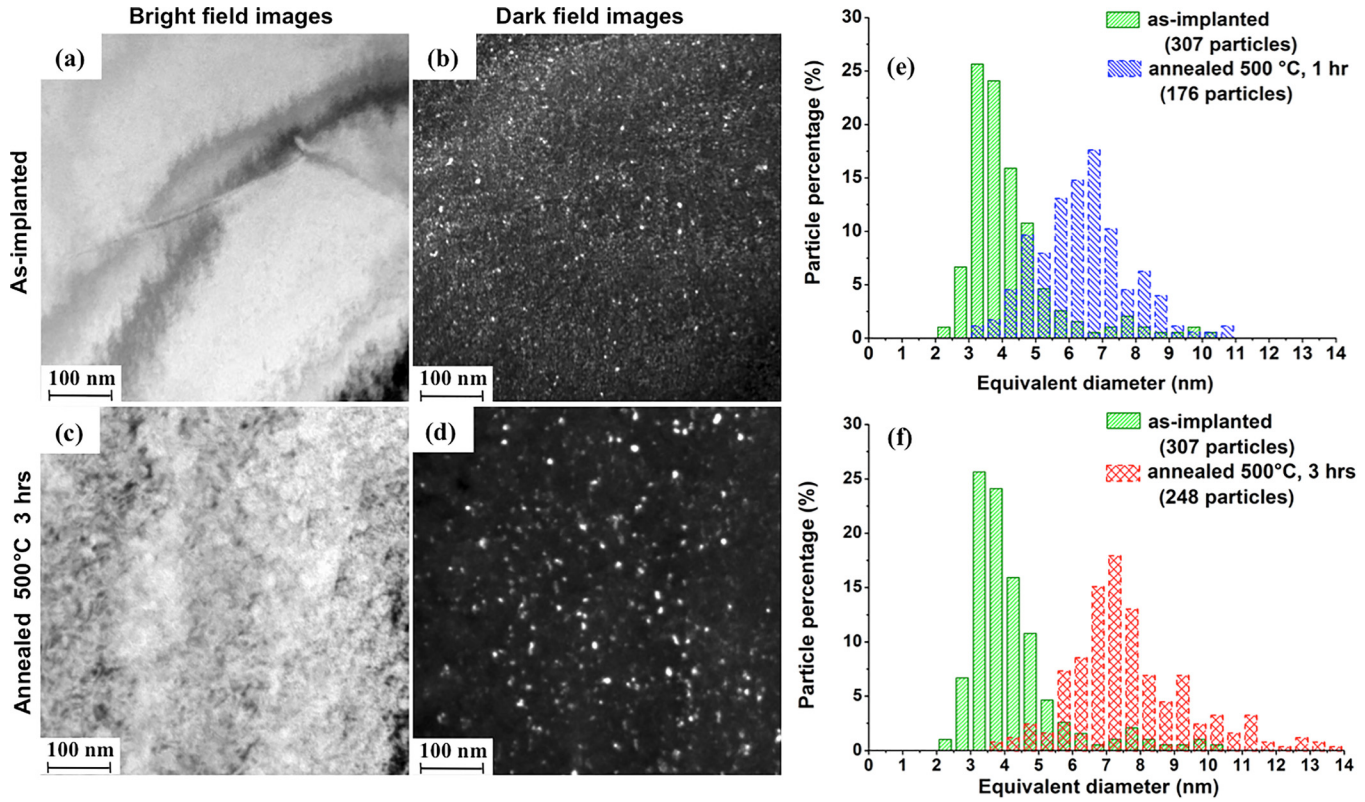

FIG. 14. (a) Bright field TEM micrograph of the as-implanted TEM thin foil. (b) Corresponding dark field TEM micrograph. (c) Bright field TEM micrograph of the annealed (3 h at 500 °C) TEM thin foil. (d) Corresponding dark field TEM micrograph. Panels (e) and (f) show histograms of the size distributions for nano-particles identified from images (b) and (d), respectively.

number density of precipitates in the as-implanted sample was estimated to be $(1 \pm 0.3) \times 10^{22}\,m^{-3}$, whereas that in the sample annealed for 3 h was $\sim(7 \pm 2) \times 10^{21}\,m^{-3}$. Having in mind that the TEM images used for the estimation correspond to different sample locations with very probably somewhat different thicknesses, we can conclude that there seems to be no substantial effect of the annealing on the precipitate number density. It is clear, however, that no strong nucleation of new oxide particles during the annealing took place.

Similar to as-implanted samples, one observes a trend for the oxide precipitates to be associated with the point defect sinks. The size of precipitates at dislocation loops increases significantly as compared to those in as-implanted specimens. An example of dislocation loop decoration with oxide particles in the annealed sample is given in Fig. 15.

3. Particle chemical composition after annealing

a. EFTEM analysis. In order to clarify the possible compositional variations associated with the particle growth during the thermal annealing, the EFTEM investigation was applied to a relatively large precipitate ($d \cong 20$ nm) of presumably cubic shape, shown in Fig. 16(a). The precipitate was located in the zone, where the thickness L of the foil was sufficiently small (appr. 35 nm, as deduced from the measured ratio $L/\lambda \sim 0.32$ and the inelastic mean free path λ of $\sim$110 nm). The resulting gray scale energy-filtered images for Fe, Cr, and Al edges are presented in Figs. 16(b)–16(d). Similar to Fig. 5, the color images of element distribution on top of iron are given in the second row of Fig. 16. The dark contrast on the Fe-$M_{2,3}$ elemental map, see Figs. 16(b) and 16(e), evidences the local Fe depletion, enabling clear positioning of the precipitate in the matrix. The element distribution maps acquired by the filtering of the Cr-$M_{2,3}$ and Al-$L_{2,3}$ edges exhibit the spots of bright contrast that coincide with the dark area in the Fe elemental map. A similar result is observed for O-K edge in Fig. 16(h). All these observations suggest that the precipitates remain (Al,Cr) oxides after thermal annealing.

b. APT measurements. In order to clarify the effect of annealing on the chemical composition of newly created clusters, the atomic probe tomography analysis was undertaken on several tips cut from the annealed sample. Due to the relatively small tip diameter, the analyzed volumes contain mostly small clusters (with the size of only several nanometers), which are present at large enough concentrations and provide information about the depth distribution and chemical composition of these clusters. Here the cluster analysis was applied to a sub-volume of approximately $40 \times 40 \times 110\,nm^3$, located at depths between 90 and 230 nm from the TEM sample surface (or, more precisely, from the tip interface with the Ni capping layer), as shown in Fig. 13(a). The subvolume was selected sufficiently deep under the TEM foil surface not to be influenced by the noticeable surface oxidation that took place during the annealing, as evidenced both by the strong sub-surface oxygen enrichment

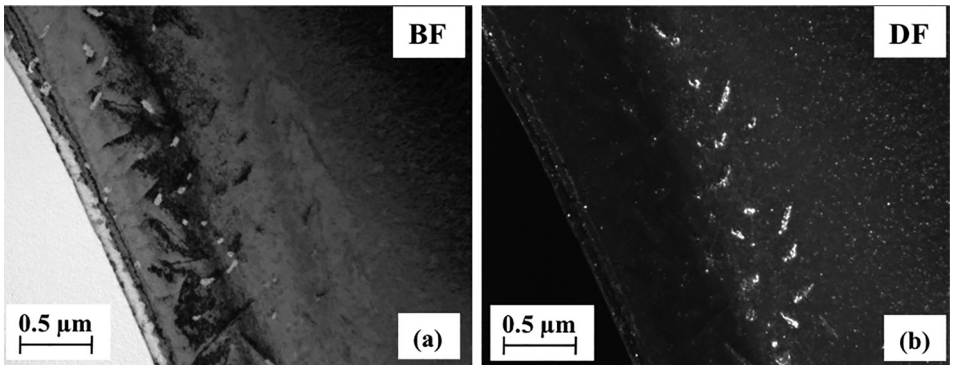

FIG. 15. TEM micrographs showing the precipitation at dislocation loops after the thermal annealing. (a) BF TEM micrograph; (b) corresponding DF TEM micrograph.

(measured on the same APT tip) and by the presence of large metal-oxide fragments (identified by diffraction measurements and APT 3D reconstruction as magnetite or chromite) in TEM foil under the surface oxide layer; see Fig. 13. At intermediate thickness (30–100 nm), the clusters were interconnected and it was not possible to identify them. Looking at Fig. 13, one can notice that the studied volume is located behind the ion implantation profile peaks and becomes noticeably enriched in both Al and O already as a result of annealing. Hence, it can be expected that the clusters observed in this area had been mainly nucleated at the annealing stage.

The measured mass spectrum of sputtered atoms demonstrates numerous peaks corresponding not only to single elements (Fe, Cr, Al, and O), but also to small metal-oxygen fragments (FeO, Fe_2O, CrO, CrO_2, AlO, and AlO_2). The distributions of evaporated elemental species (Fe, Cr, Al, and O) and molecular ions corresponding to oxides (CrO and AlO) in the studied sub-volume are shown in Fig. 17. The overall elemental content was found to be 87.41 ± 0.06 at. % Fe, 10.37 ± 0.09 at. % Cr, 0.59 ± 0.06 at. % Al, and 1.49 ± 0.09 at. % O. The distributions of iron and chromium are almost uniform over the volume, similar to the as-implanted tip, allowing no indication of cluster-related Fe and Cr variations at this background. But precipitates can be observed clearly in the charts for CrO and Al + O + AlO; see Fig. 17. Therefore, the cluster analysis algorithm was applied considering only elemental species (Al, O) and molecular fragments corresponding to aluminum oxide contribution (Al_2O, AlO, and O_2).

Altogether 165 clusters were identified in the studied sub-volume, corresponding to the cluster number density of $\sim 4.9 \times 10^{23}\,m^{-3}$, much larger than the number of clusters visible in TEM. The depth distribution of clusters is pronouncedly non-uniform, see Fig. 18(a), with the peak at the depth of ~130 nm, well behind the implanted ion profiles. The clusters are quite small, with the average size (defined in terms of effective radius) equal to ~3.4 nm; see Fig. 18(b).

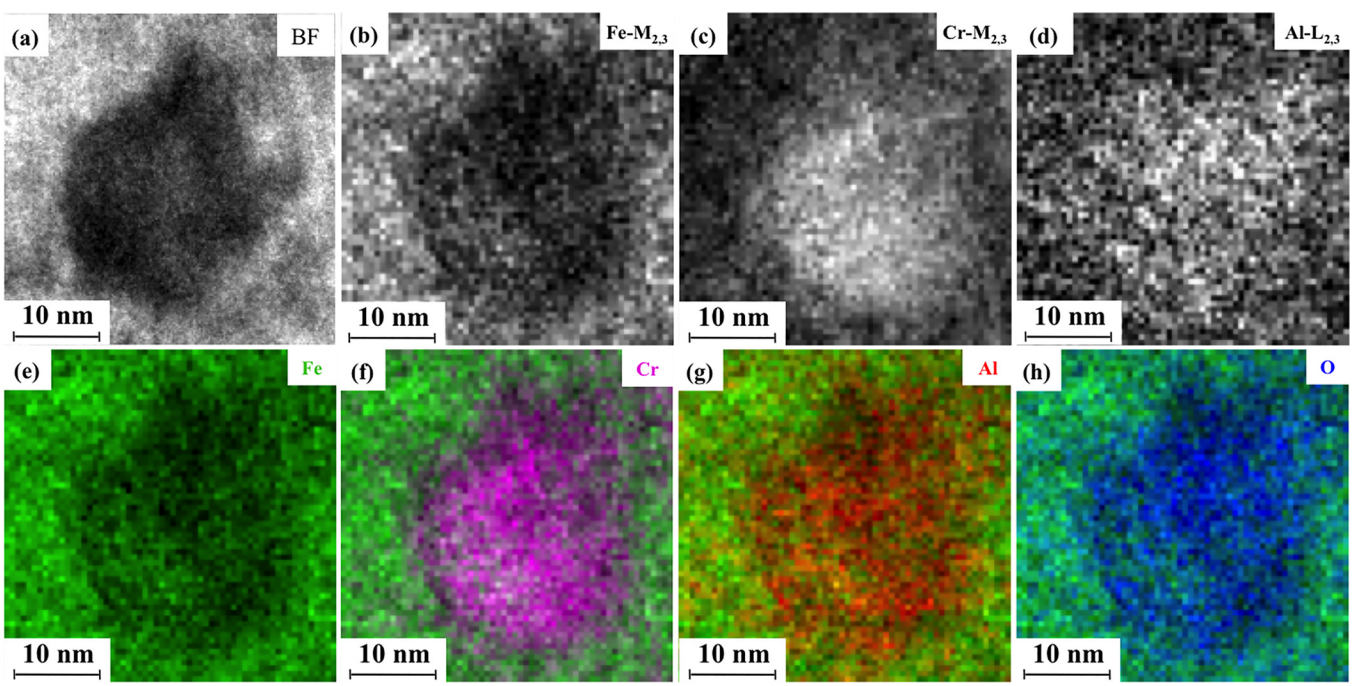

FIG. 16. EFTEM characterization of nano-particles: (a) bright field TEM image of the region of interest for the characterization. A possible nano-particle is surrounded by the square. EFTEM jump ratio images acquired on Fe-$M_{2,3}$ (b), Cr-$M_{2,3}$ (c), and Al-$L_{2,3}$ (d) edges. The comparison among jump ratio images showing correlation between Fe depletion (e) and Al-Cr-O enrichment (f)–(h) after thermal annealing. The colors indicate the elements as marked in the legend.

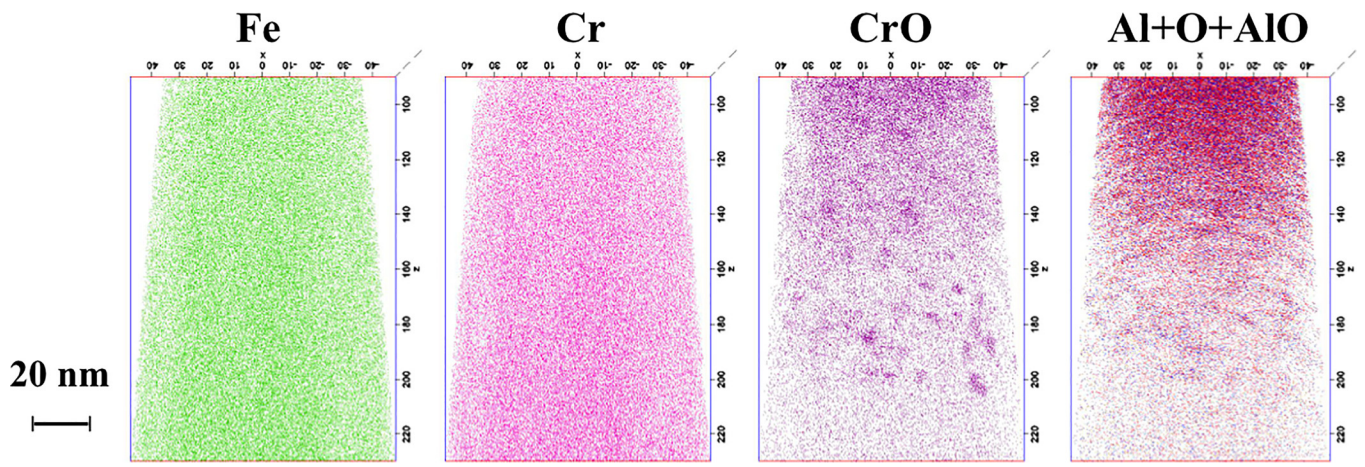

FIG. 17. 3D APT reconstruction from the annealed tip showing the distribution of evaporated elements and molecular fragments.

The level of Fe measured in the clusters varies from 70% to 87%, indicating more pronounced iron depletion in cluster areas as compared to the as-implanted case. The overall elemental content in the selected sub-volume matrix was found to be 88.94 ± 0.03 at. % Fe, 10.51 ± 0.09 at. % Cr, 0.17 ± 0.06 at. % Al, and 0.38 ± 0.06 at. % O; however, the overall element content in all studied clusters is listed in Table I. The concentrations of core elements Al and O are, respectively, 23.5 and 9 times higher than those measured from the matrix. The concentration of Cr in the clusters is 20% higher than that measured from the matrix.

The Cr, Al, and O contents for each of 165 studied clusters are shown in Fig. 19. The contents of Al and O in all clusters are significantly higher than those in the matrix. However, this is not always the case for the Cr content in the clusters and ~10% of the clusters have a lower Cr content than the matrix. However, in most clusters, the enrichment in Cr is more pronounced, as compared to the as-implanted sample. The effect is especially pronounced at depths behind the zone of intensive cluster nucleation (i.e., at depths >160 nm), where the Cr content in clusters can reach as much as 20 at. % The reason for this effect is currently unclear. Moreover, the Cr content in the clusters increases as the depth from the surface increases.

In summary, the APT results indicate that the small clusters formed at the annealing stage are rich in Al, Cr, and O, which is consistent with the results obtained in annealed thin foils by EFTEM.

As already discussed in Section III A 2 b, a large part of matrix element content observed by APT in the oxide clusters can be artificial due to trajectory aberration effects. Hence, similar to as-implanted samples, the matrix correction procedure was applied to the clusters selected in the annealed sample.

The histograms of measured and matrix-corrected elemental content in the clusters identified in the analyzed area of the annealed tip are shown in Figs. 8(c) and 8(d) as a function of the cluster effective radius. In contrast to the as-implanted sample shown in Fig. 8(b), the Al/Cr ratio after the correction has a trend to increase from 0.8 to 3.27 as the cluster size grows from 1 to 3 nm, suggesting that the cluster growth is caused preferentially by Al accumulation.

IV. DISCUSSION

The experiments on ion beam synthesis of oxide particles in the iron-chromium alloy have revealed a number of unexpected observations. First of all, quite unusual was the nucleation of oxide clusters already at the ion implantation stage. In a common scheme of ion beam synthesis, an additional post-implantation heat treatment is applied in order to develop the implant-based precipitate ensembles. Also in our experiment, the application of post-implantation annealing at 500 °C has led to remarkable development of the oxide precipitate system. However, the main mode of precipitate ensemble development was the precipitate coarsening, rather than the nucleation of new precipitates. The new particle precipitation was pronounced only at the periphery of the implanted element profiles, where both Al and O appeared as a result of diffusion already at the annealing stage.

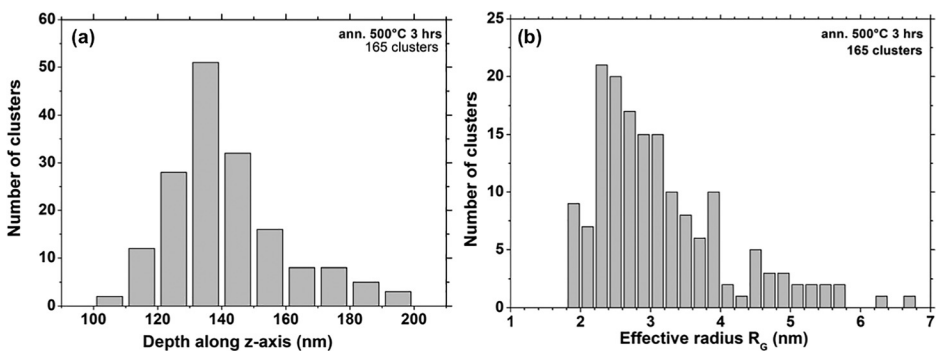

FIG. 18. (a) The depth distribution of cluster center positions in the studied volume of APT sample. (b) The size distribution of identified clusters in the same area.

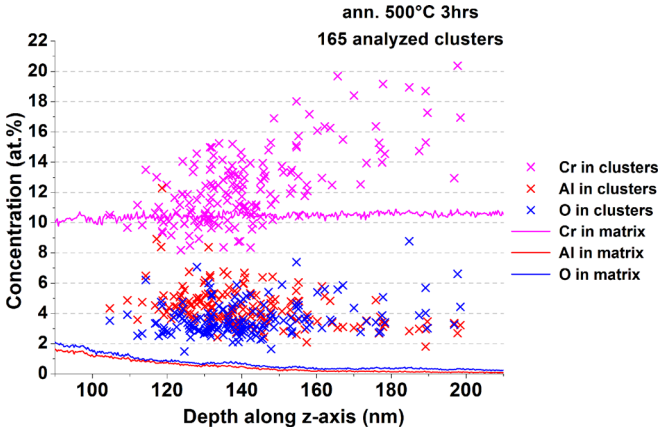

FIG. 19. The evolution of cluster elemental contents as a function of the cluster depth position (measured from the tip interface with the capping layer). Cross symbols with different colors mark atomic compositions of Cr, Al, and O in the clusters, as specified in the legend. Elemental compositions in the matrix are shown with solid color lines.

Another unusual feature was the observed crystal structure of the oxide precipitates. Although the ground state of $(Al,Cr)_2O_3$ is the hexagonal corundum structure, the electron diffraction pattern from the precipitates corresponded to a cubic structure (most probably, fcc). Whereas several metastable cubic modifications of alumina are known, the spinel-based structure, traditionally assigned to these modifications, is not compatible with the HRTEM observations. On the other hand, the observed HRTEM images do not contradict to several other known cubic structures of metal sesquioxides, though none of those considered in this paper were able to fully describe all the details. These results indicate that the nucleation of oxide particles under and after ion implantation is influenced by geometrical restrictions imposed by the host Fe-Cr matrix. This conclusion is strongly supported by the discovered orientational correlations of oxide and matrix lattices.

In order to explain these observations, we suggest a tentative set of mechanisms that can provide a consistent picture of the (Al,Cr) oxide particle synthesis in our experimental setup.

First of all, the precipitation of impurities introduced in the material by ion implantation requires sufficiently high rates of mass transport. The fast thermally activated diffusion of both Al and O atoms at the annealing stage could be expected and was indeed directly confirmed by APT measurements. The observation of cluster formation at the ion implantation stage at room temperature also implies sufficiently fast transport of both implanted components, which is, evidently, provided by primary radiation defects that are abundantly produced by ion implantation (several hundreds of Frenkel pairs per implanted ion, according to SRIM-based estimates). Indeed, according to our earlier estimates,[6] the mobility of created point defects should be sufficient to allow the Al atom transport to the newly formed clusters.

The two-stage implantation scheme in our experiments was such that Al atoms were implanted first. It was natural to ask whether cluster precipitation occurred already at this stage or is postponed until the oxygen is implanted. The experiment with the implantation of only Al ions clearly evidences the formation of precipitates (see Fig. 2). These precipitates demonstrate fcc-like reflections on the electron diffraction images and are tentatively interpreted either as pure aluminum clusters or, more probably, as the intermetallic Fe-Al phase (the exact identification requires additional analysis to be reported elsewhere).

The fact that the precipitation starts already at the first implantation stage is a key to understanding why the precipitation is preferentially observed at such microstructural features as dislocations and grain boundaries. Indeed, Al is known to be soluble in pure iron at concentration up to 17–20 at. %,[46] whereas the concentration of Al atoms even in the peak of implantation profile was <5 at. %. Hence, it is hard to expect Al precipitation in the bulk. On the other hand, the radiation-enhanced diffusion often promotes segregation of impurities to point defect sinks, especially to grain boundaries;[47] observations of radiation-induced segregation in ferritic/martensitic steels under both ion and neutron irradiation are frequently reported in the literature (e.g., Refs. 48–50). The local enrichment of Al at extended defects in our case was indeed observed and confirmed by EFTEM. This enrichment seems to be sufficient to promote the precipitation of Al-enriched phase (presumably $D0_3$ modification of Fe_3Al phase with fcc Al sublattice) at these point defect sinks. The precipitation of a new phase can be accelerated by the presence of large numbers of radiation-induced vacancies because the formation of small Al-vacancy clusters is highly profitable in terms of the energy gain.[51]

Correspondingly, the correlated distribution of oxide particles along dislocations and grain boundaries implies that oxygen implanted at the second implantation stage is captured preferentially by already formed Al-enriched clusters. Indeed, Al-enriched clusters should capture sufficiently large numbers of vacancies because the vacancy formation energy at the iron sublattice in Fe_3Al is notably lower than that in the bulk.[52] An additional indication in the same direction comes from first principle simulations[51] indicating that small Al-vacancy clusters (with at least up to four Al atoms and/or vacancies) prefer to have compact form with Al atom located on iron lattice positions following the fcc pattern and with vacancies in between the Al atoms, so that no iron is left inside the clusters. The vacancies in the Al-enriched clusters are natural traps for oxygen atoms and promote oxygen accumulation in clusters that results in the conversion of intermetallic clusters into oxides. In fact, one might expect that the conversion can occur gradually either as a result of the vacancy accumulation on the iron sites in the intermetallic phase, followed by filling the captured vacancies with oxygen atoms, or by simultaneous acquisition of vacancies and oxygen atoms by capturing vacancy-oxygen pairs that, according to Ref. 4, provide the fastest oxygen diffusion mode in iron below the Curie temperature.

While needing confirmation by further experimental studies and quantitative modeling, the suggested scenario of oxide cluster formation gives a natural explanation of the unusual features summarized in the starting paragraphs of this section.

(i) The particle lattice alignment with the host lattice is simply a consequence of Al sublattice in the intermetallic phase being formed "on top" of the iron lattice.
(ii) The fcc-based cubic structure of the oxide results from the fact that it is inherited from the Al skeleton in the original intermetallic phase. Even though this cubic phase is not thermodynamically stable, it cannot spontaneously transform into hexagonal corundum because of both the relatively low temperature in our experiments (the transformation of cubic $(Al,Cr)_2O_3$ to corundum requires heating to at least 900 °C (Refs. 34 and 35)) and the necessity to accommodate relatively large lattice strains accompanying the transformation from cubic to hcp oxide modification.
(iii) The relatively high share of iron in the composition of very small Al-enriched clusters observed by APT can be explained, apart from aberration effects discussed in Sec. III A 2 b, by the fact that iron is eliminated from clusters only gradually, as a result of vacancy accumulation and their subsequent filling with oxygen.
(iv) One can also speculate that the particle enrichment in Cr, which persists even after the high-temperature annealing, is caused by the energetics of vacancy accumulation in the intermetallic Al-enriched phase. Indeed, in our experiments, the matrix already contains ∼10 at. % Cr. As revealed by APT measurements, the absolute content of Cr in small precipitates remains at about the same level as it was in the matrix. It may well be that the vacancies that accumulate in Al-enriched clusters preferentially eliminate Fe atoms from the cluster volume, leaving Cr atoms in place, or forcing them to incorporate into the fcc Al sublattice.

V. CONCLUSIONS

(i) Some interesting features of clusters in the as-annealed samples have been found in addition to those reported earlier.[6,7] In particular, the important role of structural imperfections (dislocations and grain boundaries) in the formation of oxide particles has been demonstrated.
(ii) The unusual cubic lattice structure of the oxide precipitates was studied in detail using HRTEM and the obtained HRTEM images were compared with those simulated for a number of potentially possible structures of aluminum or chromium oxides. The comparison shows that the particle crystal structure is most probably different from that of spinel, which is commonly ascribed to the known cubic polymorphs of aluminum oxide. Among the other tested lattice structures, the most close fit to experimental images gave rocksalt (as for CrO) and rocksalt-based configurations, though none was able to reproduce all the observed fine HRTEM features.
(iii) The study has elucidated the effects of high-temperature annealing on the development of the metal-oxide precipitate system created by consecutive implantation of aluminum and oxygen ions into the pure alloy Fe-10%Cr. It was found that the precipitates formed at the ion implantation stage mostly grow, whereas new oxide precipitates nucleate at sample depths well behind the implanted ion profiles. This nucleation is ascribed to the thermal diffusion of aluminum and oxygen atoms. The clusters are found to be (Cr,Al) oxides with varying Al to Cr content ratios.
(iv) A qualitative scenario of metal-oxide precipitation during and after ion implantation has been suggested that allows us to non-contradictory explain practically all the unusual effects accompanying the development of oxide clusters in out experiment.

ACKNOWLEDGMENTS

SCALP/JANNuS-Orsay technical staff at CSNSM is acknowledged for assistance during experiments, especially C. Baumier and J. Bourçois. The authors acknowledge financial support from the CNRS-CEA "METSA" French network (FR CNRS 3507) for the Atom Probe experiments conducted on the IM2NP platform. Partial financial support from IN2P3 Institute (AP ODS) and the financial support from the collaborative grant of CNRS-PRC-06541 and RFBR-15-58-15002 are also essential for this project. This work received assistance from the "Agence Nationale de la Recherche" program referenced as ANR-11-EQPX-0020 (FIB).

[1]S. Ukai, "Oxide dispersion strengthened steels," in *Comprehensive Nuclear Materials*, edited by R. J. M. Konings (Elsevier, Amsterdam, 2012), Vol. 4, p. 241.
[2]E. A. Marquis, Appl. Phys. Lett. **93**, 181904 (2008).
[3]D. Murali, B. K. Panigrahi, M. C. Valsakumar, S. Chandra, and C. S. Sundar, J. Nucl. Mater. **403**, 113 (2010).
[4]C. L. Fu, M. Krčmar, G. S. Painter, and X.-Q. Chen, Phys. Rev. Lett. **99**, 225502 (2007).
[5]J. Xu, C. T. Liu, K. Miller, and H. Chen, Phys. Rev. B **79**, 020204 (2009).
[6]C. Zheng, A. Gentils, J. Ribis, O. Kaïtasov, V. A. Borodin, M. Descoins, and D. Mangelinck, Philos. Mag. **94**, 2937 (2014).
[7]C. Zheng, A. Gentils, J. Ribis, V. A. Borodin, O. Kaïtasov, and F. Garrido, Nucl. Instrum. Methods Phys. Res., Sect. B **365**, 319 (2015).
[8]D. Sakuma, S. Yamashita, K. Oka, S. Ohnuki, L. E. Rehn, and E. Wakai, J. Nucl. Mater. **329**, 392 (2004).
[9]J. Chao, Mater. Sci. Eng., A **242**, 248 (1998).
[10]M. K. Miller, D. T. Hoelzer, E. A. Kenik, and K. F. Russell, J. Nucl. Mater. **329**, 338 (2004).
[11]D. Sporer and G. Korb, Met. Powder Rep. **47**(2), 62 (1992).
[12]J. F. Ziegler, J. P. Biersack, and U. Littmark, *The Stopping and Range of Ions in Solids* (Pergamon Press, New York, 1996).
[13]N. Juslin, K. Nordlund, J. Wallenius, and L. Malerba, Nucl. Instrum. Methods Phys. Res., Sect. B **255**, 75 (2007).
[14]C. Zheng, A. Gentils, J. Ribis, V. A. Borodin, L. Delauche, and B. Arnal, "Nano-size metallic oxide particle synthesis in Fe-Cr alloys by ion implantation," Nucl. Instrum. Methods Phys. Res., Sect. B (in press).
[15]B. Gault, D. Haley, F. de Geuser, M. P. Moody, E. A. Marquis, D. J. Larson, and B. P. Geiser, Ultramicroscopy **111**, 448 (2011).
[16]D. Mangelinck, F. Panciera, K. Hoummada, M. El Kousseifi, C. Perrin, M. Descoins, and A. Portavoce, Microelectron. Eng. **120**, 19 (2014).
[17]D. Vaumousse, A. Cerezo, and P. J. Warren, Ultramicroscopy **95**, 215 (2003).
[18]E. A. Marquis and J. M. Hyde, Mater. Sci. Eng., R **69**, 37 (2010).
[19]C. A. Williams, E. A. Marquis, A. Cerezo, and G. D. W. Smith, J. Nucl. Mater. **400**, 37 (2010).

[20]D. B. Williams and C. B. Carter, *Transmission Electron Microscopy* (Plenum Press, New York, 1996), p. 678.
[21]T. Malis, J. Electron Microsc. Tech. **8**, 193 (1988).
[22]F. Hofer, W. Grogger, G. Kothleitner, and P. Warbichler, Ultramicroscopy **67**, 83 (1997).
[23]B. Gault, M. P. Moody, J. M. Cairney, and S. P. Ringer, *Atom Probe Microscopy*, Springer Series in Materials Science Vol. 160 (Springer, New York, 2012).
[24]E. A. Marquis and F. Vurpillot, Microsc. Microanal. **14**, 561 (2008).
[25]M. Klimiankou, R. Lindau, and A. Möslang, J. Nucl. Mater. **329**, 347 (2004).
[26]A. Ramar, N. Baluc, and R. Schäublin, J. Nucl. Mater. **386**, 515 (2009).
[27]J. Ribis and Y. de Carlan, Acta Mater. **60**, 238 (2012).
[28]See http://www.jems-saas.ch/ for information on JEMS software; see also P. A. Stadelmann, Ultramiscroscopy **21**, 131 (1987).
[29]E. J. W. Verway, Zeitschrift fuer Kristallographie, Kristallgeometrie, Kristallphysik, Kristallchemie Abteilung A **91**, 65 (1935).
[30]X. S. Du, S. Hak, T. Hibma, O. C. Rogojanu, and B. Struth, J. Cryst. Growth **293**, 228 (2006).
[31]A. Khatibi, J. Palisaitis, C. Höglund, A. Eriksson, P. O. Å. Persson, J. Jensen, J. Birch, P. Eklund, and L. Hultman, Thin Solid Films **519**, 2426 (2011).
[32]B. Alling, A. Khatibi, S. I. Simak, P. Eklund, and L. Hultman, J. Vac. Sci. Technol. A **31**, 030602 (2013).
[33]A. F. Holleman and E. Wiberg, *Inorganic Chemistry* (Academic Press, San Diego, 2001).
[34]A. Khatibi, J. Lu, J. Jensen, P. Eklund, and L. Hultman, Surf. Coat. Technol. **206**, 3216 (2012).
[35]A. Khatibi, A. Genvad, E. Göthelid, J. Jensen, P. Eklund, and L. Hultman, Acta Mater. **61**, 4811 (2013).
[36]H. Najafi, A. Karimi, P. Dessarzin, and M. Morstein, Surf. Coat. Technol. **214**, 46 (2013).
[37]C. M. Koller, N. Koutná, J. Ramm, S. Kolozsvári, J. Paulitsch, D. Holec, and P. H. Mayrhofer, AIP Adv. **6**, 025002 (2016).
[38]N. B. Pilling and R. E. Bedworth, J. Inst. Met. **29**, 529 (1923).
[39]N. W. Ageew and O. J. Vher, J. Inst. Met. **44**, 83 (1930).
[40]K. Nishida, T. Yamamoto, and T. Nagata, Trans. JIM **12**, 310 (1971).
[41]J. Hirvonen and J. Räisänen, J. Appl. Phys. **53**, 3314 (1982).
[42]H. Oikawa, Tetsu-to-Hagane **68**, 1489 (1982).
[43]A. B. Campbell, B. D. Sartwell, and P. B. Needham, Jr., J. Appl. Phys. **51**, 283 (1980).
[44]R. Barlow and P. J. Grundy, J. Mater. Sci. **4**, 797 (1969).
[45]J. Takada, S. Yamamoto, S. Kikuchi, and M. Adachi, Oxid. Met. **25**, 93 (1986).
[46]U. R. Kattner, *Binary Alloy Phase Diagrams*, 2nd ed., edited by T. B. Massalski (American Society for Metals, Material Park, OH, 1990), Vol. 1, p. 147.
[47]M. Nastar and F. Soisson, "Radiation induced segregation," in *Comprehensive Nuclear Materials*, edited by R. J. M. Konings (Elsevier, Amsterdam, 2012), Vol. 1, p. 471.
[48]R. E. Clausing, L. Heatherly, R. G. Faulkner, A. F. Rowcliffe, and K. Farrell, J. Nucl. Mater. **141**, 978 (1986).
[49]Z. Jiao and G. S. Was, Acta Mater. **59**, 4467 (2011).
[50]G. S. Was, J. P. Wharry, B. Frisbie, B. D. Wirth, D. Morgan, J. D. Tucker, and T. R. Allen, J. Nucl. Mater. **411**, 41 (2011).
[51]H. Amara, C. C. Fu, F. Soisson, and P. Maugis, Phys. Rev. B **81**, 174101 (2010).
[52]R. Besson, A. Legris, D. Connetable, and P. Maugis, Phys. Rev. B **78**, 014204 (2008).